

# A versatile and transportable endstation for controlled molecule experiments

Wuwei Jin,<sup>1,2</sup> Hubertus Bromberger,<sup>1</sup> Lanhai He,<sup>1, a)</sup> Melby Johny,<sup>1,2,3</sup> Ivo S. Vinklárek,<sup>1</sup> Karol Długołęcki,<sup>1</sup> Andrey Samartsev,<sup>1</sup> Francesca Calegari,<sup>1,2,3</sup> Sebastian Trippel,<sup>1,3, b)</sup> and Jochen Küpper<sup>1,2,3, c)</sup>

<sup>1)</sup> Center for Free-Electron Laser Science CFEL, Deutsches Elektronen-Synchrotron DESY, Notkestr. 85, 22607 Hamburg, Germany

<sup>2)</sup> Department of Physics, Universität Hamburg, Luruper Chaussee 149, 22761 Hamburg, Germany

<sup>3)</sup> Center for Ultrafast Imaging, Universität Hamburg, Luruper Chaussee 149, 22761 Hamburg, Germany

(Dated: 2024-06-25)

We report on a new versatile transportable endstation for controlled molecule (eCOMO) experiments providing a combination of molecular beam purification by electrostatic deflection and simultaneous ion and electron detection using velocity-map imaging (VMI). The *b*-type electrostatic deflector provides spatial dispersion of species based on their effective-dipole-moment-to-mass ratio. This enables selective investigation of molecular rotational quantum states, conformers, and molecular clusters. Furthermore, the double-sided VMI spectrometer equipped with two high-temporal-resolution event-driven Timepix3 cameras provides detection of all generated ions independently of their mass-over-charge ratio and electrons. To demonstrate the potential of this novel apparatus, we present experimental results from our investigation of carbonyl sulfide (OCS) after ionization. Specifically, we provide the characterization of the molecular beam, electrostatic deflector, and electron- and ion-VMI spectrometer. The eCOMO endstation delivers a platform for ultrafast dynamics studies using a wide range of light sources from table-top lasers to free-electron-laser and synchrotron-radiation facilities. This makes it suitable for research activities spanning from atomic, molecular, and cluster physics, over energy science and chemistry, to structural biology.

## I. INTRODUCTION

The advancement of synchrotron and x-ray free-electron laser (XFEL) radiation sources, such as those at DESY (FLASH), the linac coherent light source (LCLS), the free-electron laser radiation for multidisciplinary investigations (FERMI), the SPring-8 Angstrom compact free-electron laser (SACLA), the x-ray free-electron laser at the Paul Scherrer Institute (SwissFEL), the European x-ray free-electron laser (EuXFEL), and the Shanghai soft x-ray free-electron laser (SXFEL), substantially pushes the boundaries of existing research areas and breaks the ground for completely new fields.<sup>1–14</sup> These sources generate ultra-short x-ray pulses spanning from tens of femtoseconds down to the attosecond range.<sup>15–17</sup> Furthermore, they provide a high peak brilliance, coherence and photon energies ranging from 5 to 250 keV.<sup>4,18–25</sup> Table-top laser systems offer unique advantages in other areas: These sources include variable-wavelength optical-parametric-amplifier (OPA)-based systems,<sup>26,27</sup> high power lasers with repetition rates up to 1 MHz using optical parametric chirped-pulse amplification (OPCPA),<sup>28,29</sup> and lasers with attosecond pulse durations.<sup>30,31</sup> Each photon source has unique properties, functions, and parameters that make it suitable for different investigations, ranging from ultrafast studies of chemical reactions over bio-molecular

dynamics to materials and life science.<sup>32–37</sup> This progress led to particular needs on user-side applications, notably atomic-level-resolution molecular dynamics experiments based on ultra-cold molecular beam methods.<sup>3,8,38–43</sup>

Molecular beams are of significant importance in physical chemistry and molecular physics as they provide a unique opportunity to obtain fundamental insights into molecular photophysics and chemical processes.<sup>44–48</sup> Whereas substantial research was conducted on isolated small molecules and atoms, investigating more complex molecular systems with molecular-level insight is still restricted by many experimental challenges.<sup>14,49,50</sup> One of these challenges is to generate well-defined ensembles of the reactant particles. In this regard, many molecular beams usually contain mixtures of isolated molecules, various molecular clusters, or multiple isomers, e. g., of chiral molecules or large biomolecules. The ability to select a particular species plays a crucial role in gaining a deeper understanding of its importance in chemical behavior that also impacts a wide range of biological processes.<sup>51–54</sup> To overcome this obstacle, the electrostatic deflector was developed to achieve spatial separation of different neutral species in ultra-cold ( $T_{\text{rot}} < 1$  K) molecular beams, ultimately obtaining pure particle ensembles.<sup>50,55–59</sup>

A second challenge is recording the molecular dynamics using experimentally accessible observables. The reaction microscope (REMI) technique, for example, provides complete, correlated, 3D velocity information of all particles detected in coincidence.<sup>14,29,60</sup> However, it is limited by low count rates, which can lead to poor statistics. High-count-rate approaches such as VMI,<sup>61</sup> provide a significant improvement in that respect. A significant drawback of VMI in high count rate conditions however is that one

<sup>a)</sup>Current address: Institute of Atomic and Molecular Physics, Jilin University, Changchun 130012, China

<sup>b)</sup>Email: sebastian.trippel@cfel.de

<sup>c)</sup>Email: jochen.kuepper@cfel.de;

Website: <https://www.controlled-molecule-imaging.org>

cannot rely on coincidence detection to extract, e. g., information about different electrons and ions coming from the same target molecule, although covariance mapping methods<sup>62</sup> can partially overcome this problem. Lastly, for VMIs, photoelectron photoion coincidence (PEPICO) spectroscopy that is synchronizing VMI- and time-of-flight (TOF) information, is also challenging.<sup>63</sup> These issues so far limit access to the full kinematics of single reactions and, therefore, systematic studies of the underlying physical mechanisms.

This article provides a comprehensive overview of the newly established endstation for controlled molecule experiments. It addresses the aforementioned challenges of the current experimental research. eCOMO provides pure, cold, dense, and pulsed molecular beams of selected species using Even-Lavie valves<sup>64</sup> in combination with the electrostatic deflector.<sup>50</sup> The endstation is equipped with a double-sided VMI spectrometer combined with high spatio-temporal-resolution Timepix3 cameras combined with the software package PymePix.<sup>65,66</sup> This lets us overcome the limitations of standard camera technology for advanced imaging experiments with high event rates.<sup>66-69</sup> Moreover, this also meets the high-frequency data acquisition requirements of various light sources with high repetition rates mentioned earlier.<sup>18,66</sup>

To demonstrate the capabilities of the novel system, we present the results of its commissioning with an optical laser in our laboratory. We used the fragmentation of OCS after strong-field ionization as a benchmark to characterize the molecular beam, the electrostatic deflector, and the electron-and-ion-VMI spectrometer.

## II. APPARATUS DESCRIPTION

### A. Vacuum system

The vacuum setup, shown schematically in the upper left corner of Figure 1, consists of four differentially pumped vacuum chambers housing the molecular beam source, the electrostatic *b*-type deflector, the double-sided VMI spectrometer, and the molecular beam dump. All chambers are mounted on rails to allow easy translation of the setup along the *z*-axis, which is parallel to the molecular beam propagation direction. The source chamber is pumped with two turbomolecular pumps (Pfeiffer Vacuum ATH2303 M), which results in a total pumping speed of  $\sim 3600$  l/s for helium. The source chamber is equipped with two quick-access DN250 CF doors (Pfeiffer Vacuum 420KTU250), enabling easy sample replacement in the Even-Lavie valve sample container.<sup>64</sup> Furthermore, the source chamber is separated from the deflector chamber with home-built automatic DN250 CF gate valve<sup>70</sup> to allow sample changes without breaking the vacuum of the deflector chamber and the spectrometer. The deflector chamber is also pumped with a turbomolecular pump with a pumping speed in the order of  $\sim 1800$  l/s for helium (Pfeiffer Vacuum ATH2303 M). Next, the VMI chamber is

pumped by two turbomolecular pumps (Pfeiffer Vacuum PM P06 302 and PM P06 312) resulting in an overall pumping speed of  $\sim 4000$  l/s for helium. Finally, the beam dump is pumped with a turbomolecular pump (Pfeiffer Vacuum PM P04 024) resulting in a pumping speed of  $\sim 470$  l/s for helium. In addition, a 250 mm diameter copper shield connected to a dewar for liquid nitrogen cooling is located in the VMI chamber to increase the pumping speed for molecules with freezing points above the liquid nitrogen temperature. The Dewar is designed such that liquid nitrogen must be refilled every  $\sim 7$  hours to keep the shield cold.

The first pre-vacuum line that provides vacuum to the source chamber and to the second low pressure pre-vacuum line, is pumped by an pre-vacuum pump (Pfeiffer Vacuum PR P00 009) with a nominal pumping speed of  $\sim 130$  m<sup>3</sup>/h. The second pre-vacuum line is pumped by a turbomolecular pump (Pfeiffer Vacuum PM P03 900) with a pumping speed of 255 l/s for helium. The second pre-vacuum line provides vacuum to the deflector-, VMI-, and beam dump chambers. This line is needed to compensate for the low helium compression ratio given for, e. g., the pumps of the VMI chamber by  $3 \times 10^5$ . When operating the molecular beam valve at a repetition rate of 100 Hz, the typical pressures in the source-, deflector-, VMI-, and beam dump chambers are  $\sim 10^{-6}$ ,  $\sim 10^{-8}$ ,  $\sim 10^{-10}$ , and  $\sim 10^{-10}$  mbar, respectively. Under such conditions, the typical pressure in the first and second pre-vacuum lines is  $\sim 10^{-3}$  and  $\sim 10^{-7}$  mbar, respectively. Further information on the vacuum system including the layout of gas lines, the interlock system with its logic to control the gate valves, and voltage power supplies, is provided in the supplementary information. The primary purpose of the interlock system is to ensure operation monitoring of the eCOMO vacuum system and to automatically protect the setup and spectrometer in case of sudden emergency situations.

### B. Molecular beam setup

The main part of Figure 1 shows the molecular beam setup. All molecular beam components including the valve, skimmers, deflector, and the knife edge are mounted on motorized translation stages in the *x-y* plane. The individual positions can therefore be adjusted perpendicular to the molecular beam propagation direction using linear feedthroughs and stepper motors (Thorlabs, DRV014), which can be controlled remotely. The maximum travel range for the whole molecular beam is  $\sim 11$  and  $\sim 12$  mm in *x*- and *y* direction, respectively. The implemented motors enable the alignment and vertical scanning of the molecular beam with respect to any general photon source, enabling the investigation of different sections of the quantum-state-dispersed molecular beam.

An Even-Lavie valve<sup>64</sup> is used to deliver the molecular beam by a supersonic expansion of 10–100 bar helium with typically a few mbar of sample molecules into vacuum.<sup>71</sup>

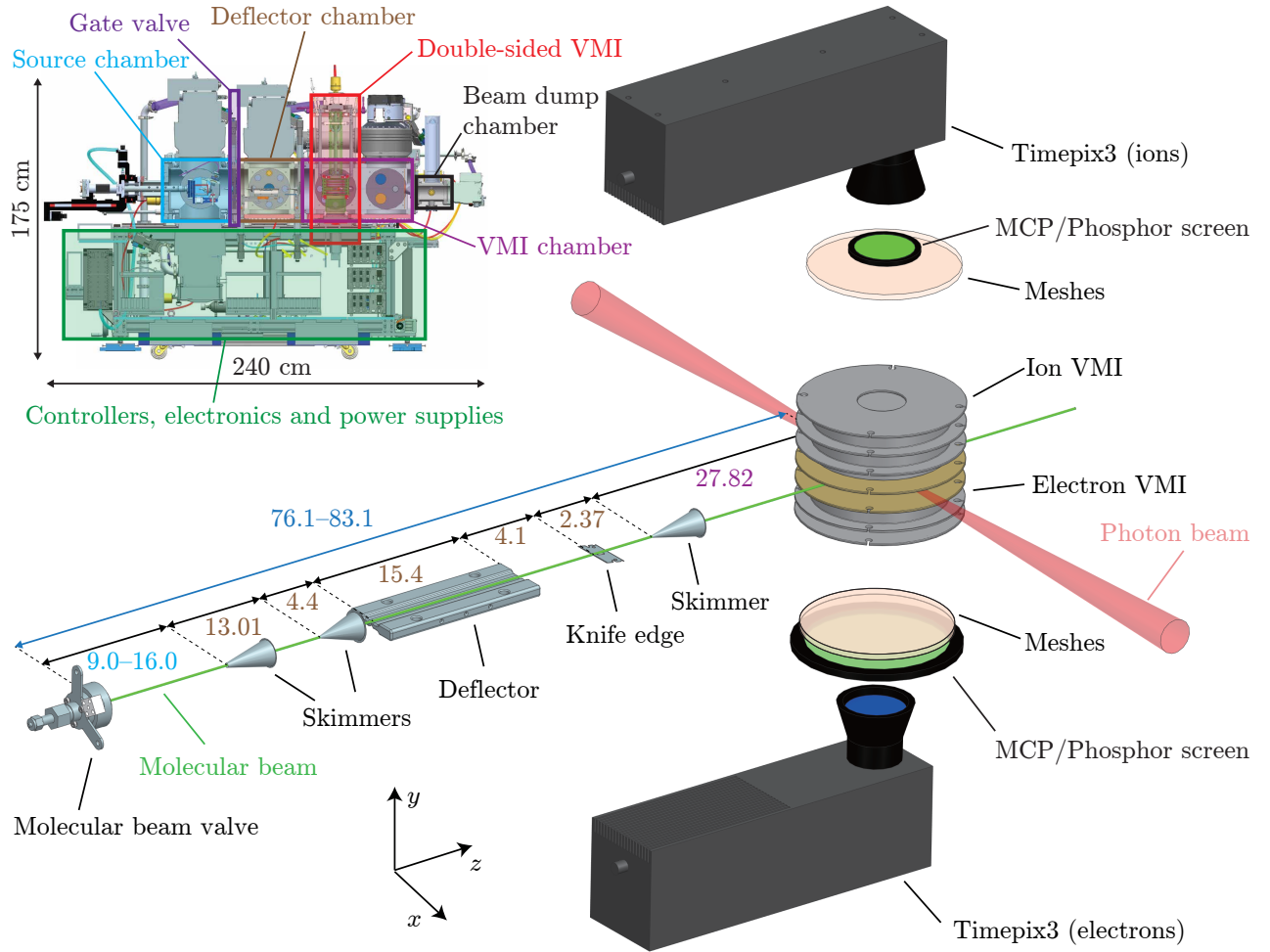


FIG. 1. Sketch of the experimental setup consisting of a molecular beam valve, an electrostatic  $b$ -type deflector, a double-sided VMI, and two Timepix3 cameras. The inset provides a side view from a CAD model, where colored frames depict the different parts of the setup. All distances are provided in cm. See text for details.

The valve temperature can be adjusted between room temperature and  $250^\circ\text{C}$  to control the vapor pressure of the sample under investigation and can be operated with a repetition rate of up to 500 Hz. The valve is mounted on a semi-motorized DN63 CF 3D manipulator (Caburn-MDC E-PSM-2504) with a travel range of 7 cm along the molecular beam propagation direction. The first conical skimmer (Beam Dynamics, model 50.8,  $\varnothing = 3$  mm) is used for skimming the molecular beam and to obtain differential pumping. The distance between the first skimmer and the valve can be adjusted between 9 and 16 cm by moving the valve along the molecular beam propagation direction. The first skimmer is mounted on a home-built flange with a built-in 2D translation stage to adjust the skimmer position in the  $x$ - and  $y$  directions. A second skimmer (Beam Dynamics, model 40.5,  $\varnothing = 1.5$  mm) is placed 13.01 cm behind the first skimmer tip for further collimation of the molecular beam. An electrostatic  $b$ -type deflector,<sup>72</sup> which disperses the molecules

in the molecular beam with respect to their quantum states<sup>50,55,57,59,73</sup> is located 4.4 cm behind the tip of the second skimmer. Both electrodes of the electrostatic deflector are connected through high-voltage feedthroughs (Pfeiffer 420XST040-30-30-1) allowing voltages of up to  $\pm 30$  kV on each electrode. The second skimmer and the electrostatic deflector are mounted together on an  $x$ - $y$  translation stage to adjust their positions. The electrostatically dispersed molecular beam is then cut by a vertically adjustable knife edge placed 4.1 cm downstream of the deflector exit. This allows for both, an improved sample separation and a higher column density of the molecular beam.<sup>74</sup> The molecular beam is further skimmed by a third conical skimmer (Beam Dynamics model 50.8,  $\varnothing = 1.5$  mm) placed 2.37 cm downstream of the knife edge, providing differential pumping against the VMI chamber. This third skimmer is again mounted on a 2D translation stage. The molecular beam enters the VMI chamber after the third skimmer. The distance

between the tip of the third skimmer and the interaction region is 27.8 cm. The state-selected molecules are ionized by the photons used for the investigation inside the double-sided VMI spectrometer.<sup>61</sup> The resulting electrons and ions are velocity-mapped onto a 120 mm (Photonis Model: APD 3 PS 120/32/25 19 I 60:1 NR 10"FM P47) and a 75 mm (Photonis Model: APD 3 PS 75/32/25/8 I 60:1 NR MGO 8"FM P47) diameter position-sensitive detectors, respectively. Each detector consists of three z-stacked multi-channel plates (MCPs) and a fast phosphor screen (P-47). Both detectors are captured by time and position-sensitive Timepix3 cameras built by Amsterdam Scientific Instruments based on homebuilt chips.<sup>66,75</sup> The molecular beam enters the beam dump chamber through a  $\varnothing = 2$  cm aperture after passing the VMI. The beam dump chamber pump is mounted with a 22 mm offset regarding the z-axis, allowing the molecular beam to directly hit onto the rotors to prevent scattering of the direct beam back into the VMI chamber.

### C. Double-sided VMI

The double-sided VMI setup specifically designed for eCOMO is illustrated in Figure 2 a along with its relevant dimensions and the electrode labels. It allows for the simultaneous detection of electrons and ions and evolved from the initial concept of velocity imaging in photoionization coincidence studies.<sup>76</sup> The VMI's adaptable design permits both, vertical and horizontal installations within the VMI chamber, facilitating flexible use in different laboratories and photon-science facilities. By default, the eCOMO spectrometer is installed vertically in the VMI chamber. However, the spectrometer can be installed alternatively horizontally along the molecular beam direction replacing the beam dump. In this case, only the long side of the spectrometer can be used for either electrons or ions. The VMI's point of origin is defined in the middle between the electrodes EE1 and IE1 as indicated by the red star. This is the location where the molecular beam interacts with the photons. Electrodes EE1 and IE1 are fabricated from oxygen-free copper (OF-Cu) with at least 5  $\mu\text{m}$  of gold plating to obtain a higher work function compared to stainless steel for experiments using high energetic photons, e. g., UV light. The remaining electrodes are made of stainless steel (1.4429 ESU), with surfaces finely polished. Additionally, a rim structure is designed around the outer edge of each electrode to reduce the influence of the VMI holder on the shape of the electric field in the center of the spectrometer. All electrodes have an outer diameter of 140 mm and are separated by ceramic spacers (Macor) as electrical insulators. A cylindrical shield surrounding the VMI, depicted in green, with holes for the photons, molecular beam, potential diagnostic paddles for x-ray experiments as well as for pumping, is composed of  $\mu$ -metal to provide shielding from stray fields and external magnetic fields. Double-layered meshes EM1–EM2 and IM1–IM2, with 80% transmission for each

Imaging mode	SMI	SVR–VMI	LVR–VMI
Electron mesh 2 (EM2)	0	-134	6864
Electron drift tube (EDT)	0	1956	9816
Electron extractor 2 (EE2)	0	490	673
Electron extractor 1 (EE1)	0	-277	-553
Ion extractor 1 (IE1)	0	-370	-593
Ion extractor 2 (IE2)	-420	-821	-4672
Ion extractor 3 (IE3)	-1600	-2373	-4717
Ion drift tube (IDT)	-1600	-2380	-4800
Ion mesh 2 (IM2)	-1600	-821	-4672

TABLE I. The voltage settings (in Volt) required for the corresponding electrodes, as displayed in Figure 2 (a) to enable the operation of the double-sided VMI in the specified modes. See text for details.

layer, are positioned on both sides of the spectrometer to ensure homogeneous drift tube fields close to the detector surfaces. The first mesh on both sides with respect to the interaction region is conductively connected to the corresponding drift tube. The VMI is completely mounted on the DN200 CF ion detector flange. Its design allows for straightforward installation or replacement entirely from the ion detector side. The electrode connections extend through wires to the DN200 CF flange, where they proceed to the exterior via electrical feedthroughs (CF16-SHV20-SH-SE-CE-NI, Vacom) with a maximum rated voltage of 20 kV each.

The spectrometer can operate in diverse photo-electron and photo-ion detection modes by adjusting the voltages across the electrodes as detailed in Table I. This table lists, as examples, the implementation of a spatial map imaging (SMI) mode<sup>77</sup> – optimized exclusively for ions – and two VMI modes for different maximum energies for the velocity components parallel to the detection plane  $E_p$ . The VMI modes images both, electron and ion velocities. Each voltage setting is tailored for specific applications. In the SMI mode, the projected position on the detector correlates with the ion's initial position and is in the first order unaffected by its initial velocity, enabling precise imaging of the ionizing region. This functionality is particularly advantageous for the alignment of the experimental setup, ensuring accurate positioning of the light focus and the molecular beam. Conversely, the VMI mode allows electrons or ions with identical velocity vectors to converge to a single spot on the corresponding detector, in the first order irrespective of their initial positions. Different VMI modes allow different maximum kinetic energies to be collected on the detector, which can be adjusted depending on the experimental situation. The detection range for the electron kinetic energy parallel to the detector surface extends up to 700 eV in the large-velocity-range VMI (LVR–VMI) mode. Single-charged ions can be mapped here with a parallel energy up to 12 eV. The range for the parallel electron kinetic energy extends up to 100 eV and for single-charged ions up to

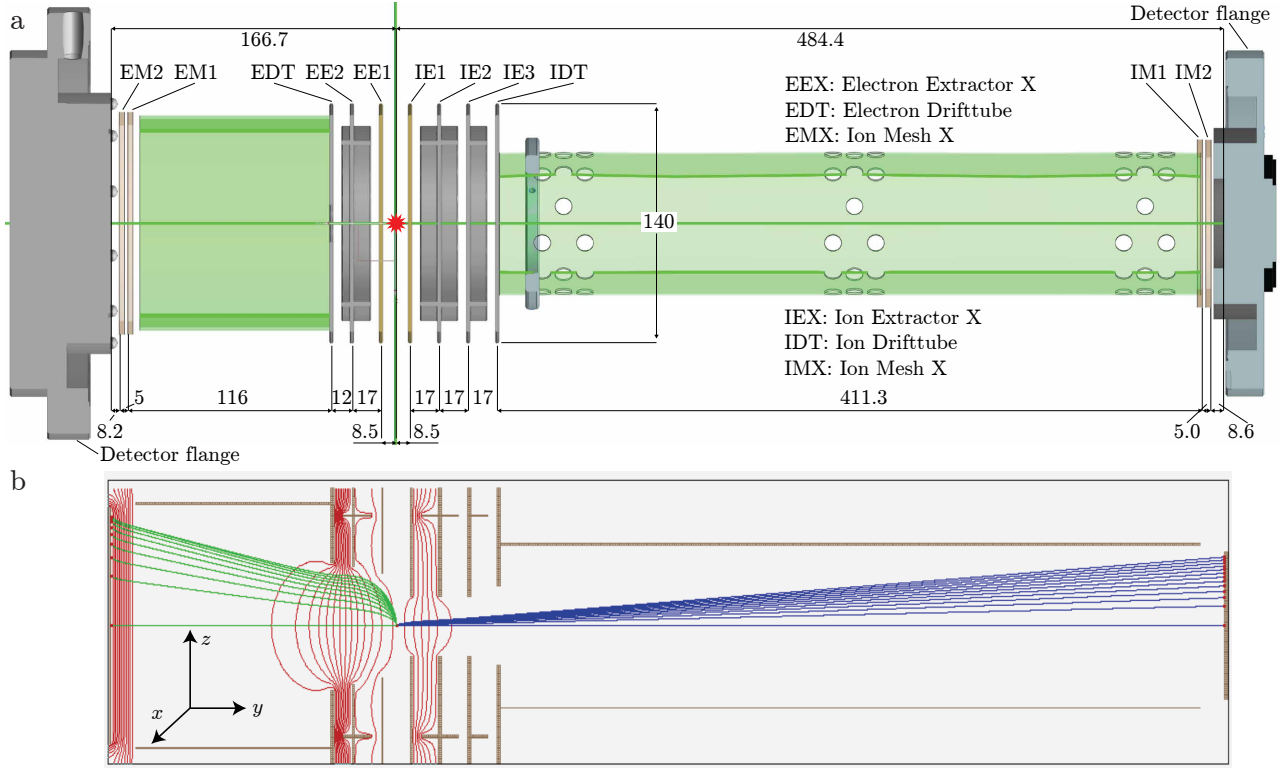


FIG. 2. (a) Schematic of the double-sided VMI setup cut along the  $y$ - $z$  plane containing the symmetry axis. The left side represents the electron detector, while the right side represents the ion detector. All distances are in mm. Typical voltage settings for each electrode can be found in Table I. The interaction region is indicated by the red star. (b) Simulation for the large velocity range mode calculated with SIMION. Equipotential lines are displayed in red. The trajectories of electrons are depicted in green, while ion trajectories are represented in blue.

10 eV in the small-velocity-range VMI mode (SVR-VMI).

The combination of MCP and phosphor screen amplifies each individual ion and electron after the particles hit the detector, by creating an avalanche of electrons that then scintillates on the phosphor screen. The light-flashes are captured with a Timepix3 camera<sup>66,67</sup> operated and controlled by our open source library PymePix.<sup>65,78</sup> PymePix is also utilized to extract the raw physics events from the Timepix3 data stream, converting them into centroided events recognized as single particle events.<sup>66</sup> The data-driven cameras, with a temporal resolution of  $\sim 1.6$  ns, enable us to operate in multi-mass detection mode and to directly obtain the VMI images of all fragments by slicing the TOF coordinate in software during analysis. The performance evaluation of the Timepix3 camera is beyond the scope of this article and was extensively discussed in other publications.<sup>66,79,80</sup> The relative positions and relative TOFs measured by the cameras can be converted to velocities in VMI conditions.

The energy resolution of the double sided VMI was determined through SIMION simulations. It is in the first approximation linearly dependent on the source size so the volume in which the ions and electrons are produced. In addition, it depends on the specific mode of spectrometer

operation. In our specific simulation we used a cylinder for the focal volume with the length given by the diameter of the molecular beam  $D = 2$  mm, and the radius given by the standard deviation of the transverse laser intensity distribution  $\sigma_r = 21$   $\mu\text{m}$  resembling our experimental conditions. Taking LVR-VMI as an example, we obtain  $\Delta E_p/E_p = 0.004$  for the ion side, which is to first order constant for all energies that can be mapped. This results in an energy resolution of  $\Delta E_p = 0.02$  eV for, e.g., a parallel ion energy of  $E_p = 5$  eV. For electrons, using the same settings, we obtain  $\Delta E_p/E_p = 0.003$ . Both resolutions are in good agreement with results obtained on similar systems.<sup>81</sup> Further settings to meet special experimental requirements are possible, but must be again found by simulations.

#### D. Portability and Installation

The eCOMO setup is designed for easy and convenient transport between different light sources, which is facilitated by four integrated wheels. Once eCOMO is positioned, four adjustable home-built support feet connected to a screw jack with standing screw (Nozag

NSE25), capable of both, horizontal and vertical adjustments, allow precise 2D positioning with a travel range of  $\pm 3$  cm. The overall height of the interaction center can be adjusted between 103 and 135 cm. The source, deflector, and VMI chambers are mounted on profile guide rails attached to the stainless steel platform by guide carriages, allowing further adjustments along the molecular beam direction. The eCOMO setup incorporates all necessary equipment, as depicted schematically in the upper left corner of Figure 1 in the green highlighted area, except for the computer used to control eCOMO and acquire data.<sup>65</sup> Integrated within the setup are all required power supplies with ports allowing quick installation, including three power cables capable of handling the necessary electrical load, a pair of inlet and outlet pipes for water circulation to cool the molecular pumps, an exhaust pipe for the vacuum system, and multiple gas sources such as nitrogen, compressed air, and the molecular carrier gas. The total weight of eCOMO including the pumps and electronics is  $\sim 1800$  kg. The overall dimensions of eCOMO are 90, 175, and 240 cm in width, height, and length, respectively.

### III. CHARACTERIZATION OF THE SETUP

#### A. Molecular beam spatial profiles

We used OCS as a sample to characterize the molecular beam and VMI performance to commission eCOMO.<sup>82,83</sup> OCS was ionized by pulses from a commercial Ti:sapphire femtosecond laser system (Coherent Astrella) operated at a repetition rate of 1 kHz. The laser beam was compressed to approximately 40 fs with a standard grating-based compression setup. The laser beam was directed through a 75 cm focal-length lens, which resulted in a peak intensity of  $I_0 \approx 3 \times 10^{14}$  W/cm<sup>2</sup>. The laser focus was spatially and temporally overlapped with the molecular beam in the interaction center of the VMI spectrometer. The pulsed molecular beam was produced by expanding a mixture of 100 bar helium and  $\sim 10$  mbar OCS. The gas mixture was expanded into the source chamber through the Even-Lavie valve operated at a temperature of 50 °C and at a repetition rate of 250 Hz. Laser shots without the molecular beam were used for background measurements. Optimized operation conditions of the valve allowed for the generation of a dense ( $> 10^7$  cm<sup>-3</sup>) molecular beam in the interaction volume. The OCS sample was displaced toward negative  $y$  positions when a total voltage of 25 kV was applied across the deflector, i. e., *de facto* the populated quantum states of OCS exhibited a strong-field-seeking character at the relevant electric field strengths in the deflector. The measured deflection profile of OCS is shown in Figure 3 as red dots. Solid lines represent simulated OCS beam profiles, computed through Monte-Carlo sampling combined with trajectory calculations that incorporate the geometrical constraints of the mechanical apertures in the experimental setup. These simulated

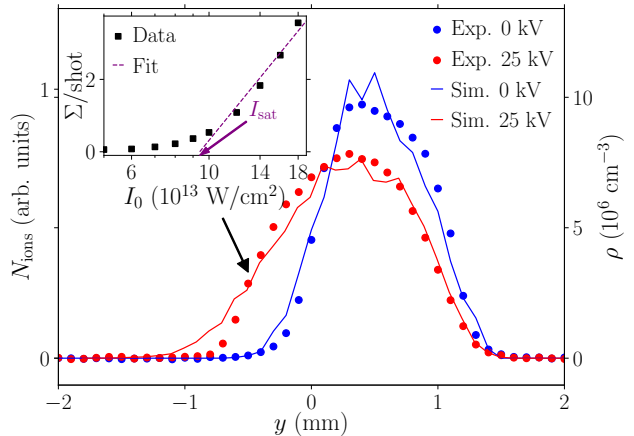


FIG. 3. Measured molecular beam density profiles (points) and simulation (solid lines) for the deflector switched off (blue) and at a total voltage of 25 kV (red) applied across the electrodes. The inset shows the number of OCS<sup>+</sup> ions  $\Sigma$  per shot (black squares) as a function of the laser peak-intensity natural logarithm  $\ln I_0$ . The purple dashed line represents the fit of the asymptotic slope. The data in the inset was measured at  $y = -0.5$  mm in the deflected molecular beam profile, marked by the black arrow.

deflection profiles of OCS match the experimental data, assuming an initial rotational temperature of  $T_{\text{rot}} = 0.5$  K for the molecular beam entering the deflector. The results affirm that the eCOMO setup can generate cold and stable molecular beams.

The OCS beam sample density was determined using a strong-field ionization model.<sup>82,84</sup> The asymptotic slope of an integral ionization signal  $\Sigma(I_0)$ , with respect to natural logarithm of the peak intensity  $\ln I_0$  approaches a limiting value as  $I_0$  approaches infinity. This slope can be expressed as:

$$\lim_{I_0 \rightarrow \infty} \left( \frac{d\Sigma}{d \ln I_0} \right) = 2\pi\alpha\sigma_r^2 D\rho \quad (1)$$

where  $\rho$  represents the sample density,  $\sigma_r$  the standard deviation of the transverse laser intensity distribution,  $\alpha$  the instrument sensitivity,  $D$  the length of the focal volume in the molecular beam, and  $\Sigma$  the total number of detected ions. The inset of Figure 3 illustrates the parent-ion signal count  $\Sigma$  per shot as a function of the laser peak intensity  $I_0$  on a semi-logarithmic scale. The data was measured at  $y = -0.5$  mm in the deflection profile as indicated by the black arrow. The asymptotic slope and saturation onset were obtained by fitting a straight line through the highest peak-intensity points, resulting in a saturation onset of  $I_{\text{sat}} = (9.4 \pm 0.3_{\text{stat}} \pm 1.9_{\text{syst}}) \times 10^{13}$  W/cm<sup>2</sup>. The subscripts indicate statistical and estimated systematic errors. This is in good agreement with the previously reported saturation intensity of OCS measured under similar experimental conditions given by  $I_{\text{sat}} = 7.2 \times 10^{13}$  W/cm<sup>2</sup>.<sup>82</sup> To extract the sample density we determined the combined sensitivity of the meshes and the MCP detector to be



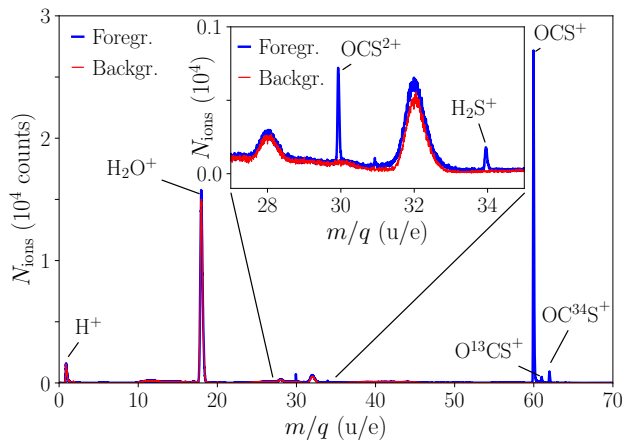


FIG. 4. TOF-MS spectrum of ions originating from the molecular beam containing OCS (blue) and from VMI-chamber background gases (red). The inset provides a magnified view of the specific region where OCS fragment ions and more highly charged ions occur.

$\alpha = 35.9\% \pm 1.3\%$  as described in Section III C. In addition we use  $\sigma_r = 21 \mu\text{m}$  and  $D = 2 \text{ mm}$  for the laser intensity standard deviation and the molecular beam width, respectively. The resulting sample density at  $y = -0.5 \text{ mm}$  is given by  $\rho = (2.86 \pm 0.58_{\text{stat}} \pm 0.57_{\text{syst}}) \times 10^6 \text{ cm}^{-3}$ . The maximum density is  $\rho \approx 10^7 \text{ cm}^{-3}$  in the direct beam as shown in Figure 3, which is one order of magnitude lower than previously reported on a similar experimental setup,<sup>82</sup> which is attributed to a lower concentration of OCS in the helium mixture.

### B. Time-of-flight mass spectrum (TOF-MS)

Figure 4 shows the time-of-flight mass spectrum (TOF-MS) resulting from strong-field ionization of OCS and from the background gas in the VMI chamber measured with the Timepix3 camera.<sup>65–67</sup> The figure displays two distinct regions: The first region depicts the OCS parent ion and its isotopologues  $\text{O}^{13}\text{CS}$  and  $\text{OC}^{34}\text{S}$ , which correspond to  $m/q = 60 \text{ u/e}$ ,  $m/q = 61 \text{ u/e}$ , and  $m/q = 62 \text{ u/e}$ , respectively. The respective signal strength is in good agreement with the corresponding natural abundance of OCS's most abundant atmospheric isotopologues.<sup>85</sup> The isotopologues with masses  $m/q = 63 \text{ u/e}$ , and  $m/q = 64 \text{ u/e}$  are also present in the data, but are not visible in the graph shown because of their natural abundance below 0.1%. The second feature is the presence of fragments, as also seen in the zoomed-in subfigure of the graph. Two broad peaks correspond to  $\text{CO}^+$  with  $m/q = 28 \text{ u/e}$  and  $\text{S}^+$  with  $m/q = 32 \text{ u/e}$  ions, which exhibit a broad ion velocity distribution due to Coulomb explosion of  $\text{OCS}^{2+}$ . The broad velocity distribution is directly reflected in the broad TOF distribution. The relatively strong background here originates from impuri-

ties of  $\text{O}_2$  and  $\text{N}_2$  gases present in the VMI chamber and the molecular beam. Additionally, two narrow peaks are observed in the inset, which correspond to doubly ionized OCS and singly ionized  $\text{H}_2\text{S}$ , which is an impurity also present in the molecular beam. The significant water ion peak can also be mostly attributed to poor background pressure conditions, which at the time, were not fully optimized and given by  $P_{\text{VMI}} = 4 \times 10^{-9} \text{ mbar}$  when the molecular beam was switched off. Additionally, there are small contributions of water ions that arose from impurities in the molecular beam. Recent modifications of the setup showed considerable improvement, achieving pressures as low as  $P_{\text{VMI}} = 3 \times 10^{-11} \text{ mbar}$ . Furthermore, the purity of the gas line was also improved by installing a cooling thermostat (ECO RE 1050 S, LAUDA).

### C. Performance of the double-sided VMI

In order to experimentally characterize the double-sided VMI, both electrons and ions from the molecular beam containing OCS were examined after strong-field ionization. Figure 5 a and Figure 5 c show the background subtracted cation-fragment velocity maps for  $m/q = 28 \text{ u/e}$  and  $m/q = 32 \text{ u/e}$ , respectively. The laser-peak-intensity here was  $I_0 = 2.5 \times 10^{14} \text{ W/cm}^2$ . The velocity maps show the commonly known features of OCS fragments after strong field ionization.<sup>83,86</sup> The central circular parts of both velocity maps are attributed to fragmentation to  $\text{CO}^+$  and  $\text{S}^+$  following single ionization. The intense central spots are attributed to  $\text{N}_2^+$  and  $\text{O}_2^+$  in the  $m/q = 28 \text{ u/e}$  and  $m/q = 32 \text{ u/e}$  velocity maps, respectively. These were impurities present in the molecular beam. The outer rings are ascribed to the Coulomb explosion channels  $\text{OCS} + nh\nu \rightarrow \text{OCS}^{+2} \rightarrow \text{CO}^+ + \text{S}^+$ . The reduced counts right above the central regions are attributed to strong signals from background ions such as  $\text{H}_2\text{O}^+$  arriving shortly before the selected ions in combination with the dead time of the Timepix3 camera.<sup>66</sup> In addition, the detector could be less sensitive there because all background ions hit this area. The projected radial velocity distributions are shown in Figure 5 e. The multiple channels corresponding to the VMIs are visible again.

The ion information can be used to determine the electron velocity map corresponding to specific ionization or fragmentation channels. To do so, both Timepix3 cameras have to be first synchronized as they independently record electrons and ions. To correlate the ion and electron cameras we simultaneously took ion and electron data at low laser intensities ( $I_0 = 3 \times 10^{13} \text{ W/cm}^2$ ) at an average event rate of 0.02 ions or electrons per shot. The number of ions  $N_i(N_{\text{trg},i})$  or electrons  $N_e(N_{\text{trg},e})$  were assigned to the camera-specific trigger numbers  $N_{\text{trg},i}$  and  $N_{\text{trg},e}$ , respectively. The normalized convolution  $N_i * N_e$  of this signal is shown in Figure 5 g as a function of the relative trigger number  $\Delta N_{\text{trg}} = N_{\text{trg},i} - N_{\text{trg},e}$ . The peak indicates the required relative trigger number shift for

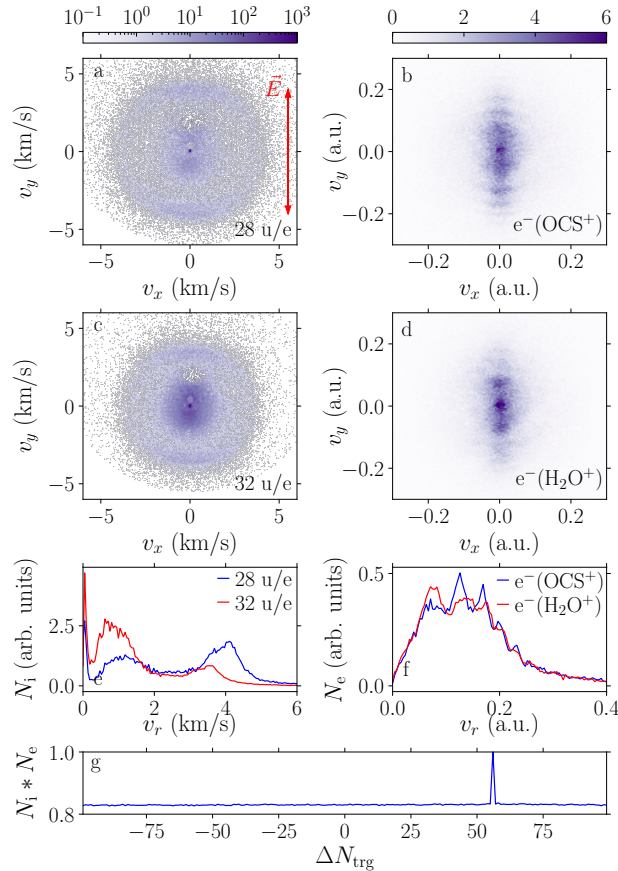


FIG. 5. (a) and (c) Projected ion velocity maps for  $m/q = 28$  u/e and for  $m/q = 32$  u/e fragments, respectively. The laser polarization is indicated by the red arrow. (b) and (d) Projected electron velocity maps for electrons correlated with  $\text{OCS}^+$  and  $\text{H}_2\text{O}^+$ , respectively. (e) and (f) Projected radial velocity distributions for ions and electrons, respectively. (g) Ion-electron Timepix3-camera-trigger correlation. See text for more details.

both cameras to be synchronized.

To demonstrate ion-electron correlations, we ionized OCS with a laser-peak-intensity of  $I_0 = 8 \times 10^{13}$  W/cm<sup>2</sup> to have both, parent ions and fragments present. In this case, the mean number of detected ions per shot was  $\sim 2$  so specific ions and electrons from single laser shots can not be correlated directly. We can, however, obtain the statistically averaged electron image using the covariance of the electron velocity maps with the boolean operation on a specific ion detected.<sup>87</sup> Figure 5 b displays the photoelectron velocity distribution after the covariance analysis where an  $\text{OCS}^+$  was measured in coincidence. The figure reveals intricate angular and radial structures as previously reported.<sup>82</sup> Specifically, the momentum distributions exhibit wide radial patterns that repeat at integer multiples of the photon energy, which is commonly referred to as above-threshold ionization (ATI). A detailed discussion about the structure of the OCS electron mo-

mentum map is beyond the scope of this manuscript and further information can be found elsewhere.<sup>82</sup> Figure 5 d displays the photoelectron momentum distribution accordingly when an  $\text{H}_2\text{O}^+$  from ionization of the background gas was measured in coincidence with an electron. A clear difference in the image structure is observed in comparison with Figure 5 b, which is attributed to the different ionization channels. The differences become even more obvious in the electron's speed distribution projected onto the detector shown in Figure 5 f. In comparison with previous work,<sup>82</sup> our short data acquisition time led to smaller experimental statistics, resulting in less detailed ATI structures. Further discussion about the underlying reason with respect to the differences in the electron velocity distributions is again beyond the scope of the manuscript. The clear differences between the two electron velocity maps however clearly show that eCOMO allows to correlate electron and ion momenta.

The low-intensity correlation measurements used for Figure 5 g enabled us furthermore to obtain the detection efficiency for electrons and ions in our setup (see SI for details). From our data we obtain a final total detection efficiency of  $\alpha_i = 35.9\% \pm 1.3\%$  and  $\alpha_e = 35.4\% \pm 1.3\%$ . Assuming a detection efficiency of the MCP given by  $\alpha_{\text{MCP}} = 50\%$  we obtain a transparency for a single mesh  $\alpha_{\text{mesh}} = 83.7\% \pm 1.5\%$ , with the estimated transmission of 80%. The deviation is attributed to the fact that the effective transmission of the second grid is higher due to the shadow cast by the first grid.

#### IV. CONCLUSIONS

In summary, eCOMO was developed, set up, and commissioned using experiments with an ultrashort-pulse table-top laser system. The performance of the cold ( $T_{\text{rot}} \leq 1$  K), pulsed, and dense ( $\rho \approx 1 \times 10^7$  cm<sup>-3</sup>) molecular beam was characterized. SIMION simulations of the double-sided VMI indicated that under experimental conditions, an energy resolution of  $\Delta E/E < 0.4\%$  is achievable. We showed that the combination of the double-sided VMI and two synchronized Timepix3 cameras at eCOMO works and that the individual ions can be separated in the data analysis based on their mass over charge ratio. Furthermore, specific molecular dynamics can be separated for systems with many fragmentation channels as shown here for OCS after ionization. Using a covariance analysis, electron VMIs and corresponding projected electron velocity distributions were assigned to specific mass over charge ratios. The absolute detection efficiency of the setup was measured by coincidence methods to  $\alpha_i = 35.9\% \pm 1.3\%$  and  $\alpha_e = 35.4\% \pm 1.3\%$  for ions and electrons, respectively. The use of the  $b$ -type electrostatic deflector allows to separate specific rotational quantum states, conformers and molecular cluster species with different effective-dipole-moment-to-mass ratios.<sup>50,72</sup> This feature of the eCOMO setup has great potential in various areas, such as the separation and purification of



complex clusters for chemical dynamics studies.<sup>53</sup>

The eCOMO setup exhibits versatile applications in the production of purified cold gas-phase molecular beams and high-precision ion-electron coincidence and covariance measurements. It can be readily adapted to a wide range of photon-source facilities, making it suitable for diverse research activities spanning atomic, molecular, and cluster physics, as well as materials science, energy science, chemistry, and biology.

## V. ACKNOWLEDGMENTS

We thank Ilya Maksimov for his experimental contributions in an early phase of the project and Daniel Gusa for technical support.

We acknowledge financial support by Deutsches Elektronen-Synchrotron DESY, a member of the Helmholtz Association (HGF), also for the provision of experimental facilities and for the use of the Maxwell computational resources operated at DESY. This research was supported by the Center for Molecular Water Science (CMWS) in an Early Science Project. The research was further supported by the Cluster of Excellence “Advanced Imaging of Matter” (AIM, EXC 2056, ID 390715994) of the Deutsche Forschungsgemeinschaft (DFG), the Helmholtz Foundation through funds from the Helmholtz-Lund International Graduate School (HELIOS, HIRS-0018), the German Federal Ministry of Education and Research (BMBF) and the Swedish Research Council (VR 2021-05992) through the Röntgen-Ångström cluster project “Ultrafast dynamics in intermolecular energy transfer: elementary processes in aerosols and liquid chemistry” (UDIET, 05K22GUA), and the European Union’s Horizon 2020 research and innovation program under the Marie Skłodowska-Curie Grant Agreement “Molecular Electron Dynamics investigated by Intense Fields and Attosecond Pulses” (MEDEA, 641789). We acknowledge CAMP@FLASH at DESY for providing some material for the spectrometer.

## VI. DATA AVAILABILITY

The data recorded in the laser lab at DESY are available from the corresponding author upon reasonable request.

## VII. CODE AVAILABILITY

The code for the data analysis is available from the corresponding author upon reasonable request.

## REFERENCES

- <sup>1</sup>R. Neutze, R. Wouts, D. van der Spoel, E. Weckert, and J. Hajdu, “Potential for biomolecular imaging with femtosecond x-ray pulses,” *Nature* **406**, 752–757 (2000).
- <sup>2</sup>J. Feldhaus, J. Arthur, and J. B. Hastings, “X-ray free-electron lasers,” *J. Phys. B* **38**, S799 (2005).
- <sup>3</sup>J. Feldhaus, M. Krikunova, M. Meyer, T. Möller, R. Moshhammer, A. Rudenko, T. Tschentscher, and J. Ullrich, “AMO science at the FLASH and European XFEL free-electron laser facilities,” *J. Phys. B* **46**, 164002 (2013).
- <sup>4</sup>M. Altarelli, R. Brinkmann, M. Chergui, W. Decking, B. Dobson, S. Düsterer, G. Grübel, W. Graeff, H. Graafsma, J. Hajdu, J. Marangos, J. Pflüger, H. Redlin, D. Riley, I. Robinson, J. Rossbach, A. Schwarz, K. Tiedtke, T. Tschentscher, I. Vartanians, H. Wabnitz, H. Weise, R. Wichmann, K. Witte, A. Wolf, M. Wulff, and M. Yurkov, “The technical design report of the European XFEL,” Tech. Rep. (DESY, Hamburg, Germany, 2007).
- <sup>5</sup>R. Neutze and K. Moffat, “Time-resolved structural studies at synchrotrons and x-ray free electron lasers: opportunities and challenges,” *Current opinion in structural biology* **22**, 651–659 (2012).
- <sup>6</sup>H. N. Chapman, A. Barty, M. J. Bogan, S. Boutet, S. Frank, S. P. Hau-Riege, S. Marchesini, B. W. Woods, S. Bajt, W. H. Benner, L. W. A., E. Plönjes, M. Kuhlmann, R. Treusch, S. Düsterer, T. Tschentscher, J. R. Schneider, E. Spiller, T. Möller, C. Bostedt, M. Hoener, D. A. Shapiro, K. O. Hodgson, D. van der Spoel, F. Burmeister, M. Bergh, C. Caleman, G. Huldt, M. M. Seibert, F. R. N. C. Maia, R. W. Lee, A. Szöke, N. Timneanu, and J. Hajdu, “Femtosecond diffractive imaging with a soft-x-ray free-electron laser,” *Nat. Phys.* **2**, 839–843 (2006).
- <sup>7</sup>B. Erk, R. Boll, S. Trippel, D. Anielski, L. Foucar, B. Rudek, S. W. Epp, R. Coffee, S. Carron, S. Schorb, K. R. Ferguson, M. Swiggers, J. D. Bozek, M. Simon, T. Marchenko, J. Küpper, I. Schlichting, J. Ullrich, C. Bostedt, D. Rolles, and A. Rudenko, “Imaging charge transfer in iodomethane upon x-ray photoabsorption,” *Science* **345**, 288–291 (2014).
- <sup>8</sup>J. Küpper, S. Stern, L. Holmegaard, F. Filsinger, A. Rouzée, A. Rudenko, P. Johnsson, A. V. Martin, M. Adolph, A. Aquila, S. Bajt, A. Barty, C. Bostedt, J. Bozek, C. Caleman, R. Coffee, N. Coppola, T. Delmas, S. Epp, B. Erk, L. Foucar, T. Gorkhober, L. Gumprecht, A. Hartmann, R. Hartmann, G. Hauser, P. Holl, A. Hömke, N. Kimmel, F. Krasniqi, K.-U. Kühnel, J. Maurer, M. Messerschmidt, R. Moshhammer, C. Reich, B. Rudek, R. Santra, I. Schlichting, C. Schmidt, S. Schorb, J. Schulz, H. Soltau, J. C. H. Spence, D. Starodub, L. Strüder, J. Thøgersen, M. J. J. Vrakking, G. Weidenspointner, T. A. White, C. Wunderer, G. Meijer, J. Ullrich, H. Stapelfeldt, D. Rolles, and H. N. Chapman, “X-ray diffraction from isolated and strongly aligned gas-phase molecules with a free-electron laser,” *Phys. Rev. Lett.* **112**, 083002 (2014), arXiv:1307.4577 [physics].
- <sup>9</sup>H. N. Chapman, C. Caleman, and N. Timneanu, “Diffraction before destruction,” *Phil. Trans. R. Soc. B* **369**, 20130313 (2014).
- <sup>10</sup>A. Rudenko, L. Inhester, K. Hanasaki, X. Li, S. J. Robotjazi, B. Erk, R. Boll, K. Toyota, Y. Hao, O. Vendrell, C. Bomme, E. Savelyev, B. Rudek, L. Foucar, S. H. Southworth, C. S. Lehmann, B. Kraessig, T. Marchenko, M. Simon, K. Ueda, K. R. Ferguson, M. Bucher, T. Gorkhober, S. Carron, R. Alonso-Mori, J. E. Koglin, J. Correa, G. J. Williams, S. Boutet, L. Young, C. Bostedt, S. K. Son, R. Santra, and D. Rolles, “Femtosecond response of polyatomic molecules to ultra-intense hard x-rays,” *Nature* **546**, 129 – 132 (2017).
- <sup>11</sup>E. Sobolev, S. Zolotarev, K. Giewekemeyer, J. Bielecki, K. Okamoto, H. K. N. Reddy, J. Andreasson, K. Ayyer, I. Barak, S. Bari, A. Barty, R. Bean, S. Bobkov, H. N. Chapman, G. Chojnowski, B. J. Daurer, K. Dörner, T. Ekeberg, L. Flückiger, O. Galzitskaya, L. Gelisio, S. Hauf, B. G. Hogue, D. A. Horke, A. Hosseinizadeh, V. Ilyin, C. Jung, C. Kim, Y. Kim, R. A. Kirian, H. Kirkwood, O. Kulyk, R. Letrun, D. Loh, M. Messerschmidt, K. Mühlig, A. Ourmazd, N. Raab, A. V. Rode, M. Rose, A. Round,

- T. Sato, R. Schubert, P. Schwander, J. A. Sellberg, M. Sikorski, A. Silenzi, C. Song, J. C. H. Spence, S. Stern, J. Sztuk-Dambietz, A. Teslyuk, N. Timneanu, M. Trebbin, C. Uetrecht, B. Weinhausen, G. J. Williams, P. L. Xavier, C. Xu, I. Vartanyants, V. Lamzin, A. Mancuso, and F. R. N. C. Maia, “Megahertz single-particle imaging at the European XFEL,” *Commun. Phys.* **3**, 97 (2020), arXiv:1912.10796 [physics].
- <sup>12</sup>J. T. O’Neal, E. G. Champenois, S. Oberli, R. Obaid, A. Al-Haddad, J. Barnard, N. Berrah, R. Coffee, J. Duris, G. Galinis, D. Garratt, J. M. Glowina, D. Haxton, P. Ho, S. Li, X. Li, J. MacArthur, J. P. Marangos, A. Natan, N. Shivaram, D. S. Slaughter, P. Walter, S. Wandel, L. Young, C. Bostedt, P. H. Bucksbaum, A. Picón, A. Marinelli, and J. P. Cryan, “Electronic population transfer via impulsive stimulated x-ray raman scattering with attosecond soft-x-ray pulses,” *Phys. Rev. Lett.* **125**, 073203 (2020).
- <sup>13</sup>S. Li, T. Driver, P. Rosenberger, E. G. Champenois, J. Duris, A. Al-Haddad, V. Averbukh, J. C. T. Barnard, N. Berrah, C. Bostedt, P. H. Bucksbaum, R. N. Coffee, L. F. DiMauro, L. Fang, D. Garratt, A. Gattton, Z. Guo, G. Hartmann, D. Haxton, W. Helml, Z. Huang, A. C. LaForge, A. Kamalov, J. Knurr, M.-F. Lin, A. A. Lutman, J. P. MacArthur, J. P. Marangos, M. Nantel, A. Natan, R. Obaid, J. T. O’Neal, N. H. Shivaram, A. Schori, P. Walter, A. L. Wang, T. J. A. Wolf, Z. Zhang, M. F. Kling, A. Marinelli, and J. P. Cryan, “Attosecond coherent electron motion in Auger-Meitner decay,” *Science* **375**, 285–290 (2022).
- <sup>14</sup>R. Boll, J. M. Schäfer, B. Richard, K. Fehre, G. Kastirke, Z. Jurak, M. S. Schöffler, M. M. Abdullah, N. Anders, T. M. Baumann, S. Eckart, B. Erk, A. De Fanis, R. Dörner, S. Grundmann, P. Grychtol, A. Hartung, M. Hofmann, M. Ichen, L. Inhester, C. Janke, R. Jin, M. Kircher, K. Kubicek, M. Kunitzki, X. Li, T. Mazza, S. Meister, N. Melzer, J. Montano, V. Music, G. Nalin, Y. Ovcharenko, C. Passow, A. Pier, N. Rennhack, J. Rist, D. E. Rivas, D. Rolles, I. Schlichting, L. P. H. Schmidt, P. Schmidt, J. Siebert, N. Strenger, D. Trabert, F. Trinter, I. Vela-Perez, R. Wagner, P. Walter, M. Weller, P. Ziolkowski, S.-K. Son, A. Rudenko, M. Meyer, R. Santra, and T. Jahnke, “X-ray multiphoton-induced Coulomb explosion images complex single molecules,” *Nat. Phys.* **18**, 423–428 (2022).
- <sup>15</sup>C. Pellegrini, A. Marinelli, and S. Reiche, “The physics of x-ray free-electron lasers,” *Rev. Mod. Phys.* **88**, 015006 (2016).
- <sup>16</sup>N. Huang, H. Deng, B. Liu, D. Wang, and Z. Zhao, “Features and futures of x-ray free-electron lasers,” *Innovation* **2**, 100097 (2021).
- <sup>17</sup>N. Hartmann, G. Hartmann, R. Heider, M. S. Wagner, M. Ichen, J. Buck, A. O. Lindahl, C. Benko, J. Grünert, J. Krzywinski, J. Liu, A. A. Lutman, A. Marinelli, T. Maxwell, A. A. Miahnahri, S. P. Moeller, M. Planas, J. Robinson, A. K. Kazansky, N. M. Kabachnik, J. Viehhaus, T. Feurer, R. Kienberger, R. N. Coffee, and W. Helml, “Attosecond time–energy structure of x-ray free-electron laser pulses,” *Nat. Photon.* **12**, 215–220 (2018).
- <sup>18</sup>W. Decking, S. Abeghyan, P. Abramian, A. Abramsky, A. Aguirre, C. Albrecht, P. Alou, M. Altarelli, P. Altmann, K. Amyan, V. Anashin, E. Apostolov, K. Appel, D. Auguste, V. Ayvazyan, S. Baark, F. Babies, N. Baboi, P. Bak, V. Balandin, R. Baldinger, B. Baranasic, S. Barbanotti, O. Belikov, V. Belokurov, L. Belova, V. Belyakov, S. Berry, M. Bertucci, B. Beutner, A. Block, M. Blöcher, T. Böckmann, C. Böhm, M. Böhnert, V. Bondar, E. Bondarchuk, M. Bonezzi, P. Borowiec, C. Bösch, U. Bösenberg, A. Bosotti, R. Böspflug, M. Bousonville, E. Boyd, Y. Bozhko, A. Brand, J. Branlard, S. Briechle, F. Brinker, S. Brinker, R. Brinkmann, S. Brockhauser, O. Brovko, H. Brück, A. Brüdgam, L. Butkowski, T. Büttner, J. Calero, E. Castro-Carballo, G. Cattalanotto, J. Charrier, J. Chen, A. Cherepenko, V. Cheskidov, M. Chiodini, A. Chong, S. Choroba, M. Chorowski, D. Churanov, W. Cichalewski, M. Clausen, W. Clement, C. Cloué, J. A. Cobos, N. Coppola, S. Cunis, K. Czuba, M. Czwalinna, B. D’Almagne, J. Dammann, H. Danared, A. d. Z. Wagner, A. Delfs, T. Delfs, F. Dietrich, T. Dietrich, M. Dohlus, M. Dommach, A. Donat, X. Dong, N. Doynikov, M. Dressel, M. Duda, P. Duda, H. Eckoldt, W. Ehsan, J. Eidam, F. Eints, C. Engling, U. Englisch, A. Er-makov, K. Escherich, J. Eschke, E. Saldin, M. Faesing, A. Fallou, M. Felber, M. Fenner, B. Fernandes, J. M. Fernández, S. Feucker, K. Filippakopoulos, K. Floettmann, V. Fogel, M. Fontaine, A. Francés, I. F. Martin, W. Freund, T. Freyermuth, M. Friedland, L. Fröhlich, M. Fusetti, J. Fydrzych, A. Gallas, O. García, L. Garcia-Tabares, G. Geloni, N. Gerasimova, C. Gerth, P. Geßler, V. Gharibyan, M. Gloor, J. Glowinkowski, A. Goessel, Z. Gołębiowski, N. Golubeva, W. Grabowski, W. Graeff, A. Grebentsov, M. Grecki, T. Grevsmuehl, M. Gross, U. Grosse-Wortmann, J. Grünert, S. Grunewald, P. Grzegory, G. Feng, H. Guler, G. Gusev, J. L. Gutierrez, L. Hagge, M. Hamberg, R. Hanneken, E. Harms, I. Hartl, A. Hauberg, S. Hauf, J. Hauschildt, J. Hauser, J. Havlicek, A. Hedqvist, N. Heidbrook, F. Hellberg, D. Henning, O. Hensler, T. Hermann, A. Hidvégi, M. Hierholzer, H. Hintz, F. Hoffmann, M. Hoffmann, M. Hoffmann, Y. Holler, M. Hüning, A. Ignatenko, M. Ilchen, A. Iluk, J. Iversen, J. Iversen, M. Izquierdo, L. Jachmann, N. Jardon, U. Jastrow, K. Jensch, J. Jensen, M. Jeżabek, M. Jidda, H. Jin, N. Johansson, R. Jonas, W. Kaabi, D. Kaefer, R. Kammering, H. Kapitza, S. Karabekyan, S. Karstensen, K. Kasprzak, V. Katalev, D. Keese, B. Keil, M. Kholopov, M. Killenberger, B. Kitaev, Y. Klimchenko, R. Klos, L. Knebel, A. Koch, M. Koepke, S. Köhler, W. Köhler, N. Kohlstrunk, Z. Konopkova, A. Konstantinov, W. Kook, W. Koprek, M. Körfer, O. Korth, A. Kosarev, K. Kosiński, D. Kostin, Y. Kot, A. Kotarba, T. Kozak, V. Kozak, R. Kramert, M. Krasilnikov, A. Krasnov, B. Krause, L. Kravchuk, O. Krebs, R. Kretschmer, J. Kreuzkamp, O. Kröplin, K. Krzysik, G. Kube, H. Kuehn, N. Kujala, V. Kulikov, V. Kuzmynych, D. L. Civita, M. Lacroix, T. Lamb, A. Lancetov, M. Larsson, D. L. Pividic, S. Lederer, T. Lensch, D. Lenz, A. Leuschner, F. Levenhagen, Y. Li, J. Liebing, L. Lilje, T. Limberg, D. Lipka, B. List, J. Liu, S. Liu, B. Lorbeer, J. Lorkiewicz, H. H. Lu, F. Ludwig, K. Machau, W. Maciocha, C. Madec, C. Magueur, C. Mafiana, I. Maksimova, K. Malcher, T. Maltezapoulos, E. Mamoshkina, B. Manschwetus, F. Marcellini, G. Marinkovic, T. Martinez, H. Martirosyan, W. Maschmann, M. Maslov, A. Mathiesen, U. Mavric, J. Meißner, K. Meissner, M. Messerschmidt, N. Meyners, G. Michalski, P. Michelato, N. Mildner, M. Moe, F. Moglia, C. Mohr, S. Mohr, W. Möller, M. Mommerz, L. Monaco, C. Montiel, M. Moretti, I. Morozov, P. Morozov, D. Mross, J. Mueller, C. Müller, J. Müller, K. Müller, J. Munilla, A. Münich, V. Muratov, O. Napoly, B. Näser, N. Nefedov, R. Neumann, R. Neumann, N. Ngada, D. Noelle, F. Obier, I. Okunev, J. A. Oliver, M. Omet, A. Oppelt, A. Ottmar, M. Oublaïd, C. Pagani, R. Paparella, V. Paramonov, C. Peitzmann, J. Penning, A. Perus, F. Peters, B. Petersen, A. Petrov, I. Petrov, S. Pfeiffer, C. Pflüger, S. Philipp, Y. Pienaud, P. Pierini, S. Pivovarov, M. Planas, E. Pławski, M. Pohl, J. Polinski, V. Popov, S. Prat, J. Prenting, G. Priebe, H. Pryscheński, K. Przygoda, E. Pyata, B. Racky, A. Rathjen, W. Ratuschni, S. Regnaud-Campderros, K. Rehlich, D. Reschke, C. Robson, J. Röver, M. Roggli, J. Rothenburg, E. Rusiński, R. Rybaniec, H. Sahling, M. Salmani, L. Samoylova, D. Sanzone, F. Saretzki, O. Sawlanski, J. Schaffran, H. Schlarb, M. Schlösser, V. Schlott, C. Schmidt, F. Schmidt-Foehre, M. Schmitz, M. Schmökel, T. Schnautz, E. Schneidmiller, M. Scholz, B. Schöneburg, J. Schultze, C. Schulz, A. Schwarz, J. Sekutowicz, D. Sellmann, E. Semenov, S. Serkez, D. Sertore, N. Shehzad, P. Shemarykin, L. Shi, M. Sienkiewicz, D. Sikora, M. Sikorski, A. Silenzi, C. Simon, W. Singer, X. Singer, H. Sinn, K. Sinram, N. Skvorodnev, P. Smirnow, T. Sommer, A. Sorokin, M. Stadler, M. Steckel, B. Steffen, N. Steinhilber-Kühl, F. Stephan, M. Stodulski, M. Stolper, A. Sulimov, R. Susen, J. Świerblewski, C. Sydlo, E. Syresin, V. Sytchev, J. Szuba, N. Tesch, J. Thie, A. Thiebault, K. Tiedtke, D. Tischhauser, J. Tolkiehn, S. Tomin, F. Tonisch, F. Toral, I. Torbin, A. Trapp, D. Treyer, G. Trowitzsch, T. Trublet, T. Tschentscher, F. Ullrich, M. Vannoni, P. Varela, G. Varghese, G. Vashchenko, M. Vasic, C. Vazquez-Velez, A. Verguet, S. Vilcins-Czvitkovits, R. Villanueva, B. Visentin, M. Viti, E. Vogel, E. Volobuev, R. Wagner, N. Walker, T. Wamsat, H. Weddig, G. Weichert, H. Weise,

- R. Wemendorf, M. Werner, R. Wichmann, C. Wiebers, M. Wiencsek, T. Wilksen, I. Will, L. Winkelmann, M. Winkowski, K. Wittenburg, A. Witzig, P. Wlk, T. Wohlenberg, M. Wojciechowski, F. Wolff-Fabris, G. Wrochna, K. Wrona, M. Yakopov, B. Yang, F. Yang, M. Yurkov, I. Zagorodnov, P. Zalden, A. Zavadtsev, D. Zavadtsev, A. Zhirnov, A. Zhukov, V. Ziemann, A. Zolotov, N. Zolotukhina, F. Zummack, and D. Zybin, "A MHz-repetition-rate hard x-ray free-electron laser driven by a superconducting linear accelerator," *Nat. Photon.* **14**, 391–397 (2020).
- <sup>19</sup>W. Ackermann, G. Asova, V. Ayvazyan, A. Azima, N. Baboi, J. Bähr, V. Balandin, B. Beutner, A. Brandt, A. Bolzmann, R. Brinkmann, O. I. Brovko, M. Castellano, P. Castro, L. Catani, E. Chiodroni, S. Choroba, A. Cianchi, J. T. Costello, D. Cubaynes, J. Dardis, W. Decking, H. Delsim-Hashemi, A. Delsierieys, G. Di Pirro, M. Dohlus, S. Düsterer, A. Eckhardt, H. T. Edwards, B. Faatz, J. Feldhaus, K. Flöttmann, J. Frisch, L. Fröhlich, T. Garvey, U. Gensch, C. Gerth, M. Görler, N. Golubeva, H. J. Grabosch, M. Grecki, O. Grimm, K. Hacker, U. Hahn, J. H. Han, K. Honkavaara, T. Hott, M. Hüning, Y. Ivanisenko, E. Jaeschke, W. Jalmuzna, T. Jezynski, R. Kammering, V. Katalov, K. Kavanagh, E. T. Kennedy, S. Khodyachykh, K. Klose, V. Kocharyan, M. Körfer, M. Kollwe, W. Koprek, S. Korepanov, D. Kostin, M. Krassilnikov, G. Kube, M. Kuhlmann, C. L. S. Lewis, L. Lilje, T. Limberg, D. Lipka, F. Löhler, H. Luna, M. Luong, M. Martins, M. Meyer, P. Michelato, V. Miltchev, W. D. Möller, L. Monaco, W. F. O. Müller, O. Napieralski, O. Napoly, P. Nicolosi, D. Nölle, T. Nuñez, A. Oppelt, C. Pagani, R. Paparella, N. Pchalek, J. Pedregosa-Gutierrez, B. Petersen, B. Petrosyan, G. Petrosyan, L. Petrosyan, J. Pflüger, E. Plönjes, L. Poletto, K. Pozniak, E. Prat, D. Proch, P. Pucyk, P. Radcliffe, H. Redlin, K. Rehlich, M. Richter, M. Roehrs, J. Roensch, R. Romaniuk, M. Ross, J. Rossbach, V. Rybnikov, M. Sachwitz, E. L. Saldin, W. Sandner, H. Schlarb, B. Schmidt, M. Schmitz, P. Schmüser, J. R. Schneider, E. A. Schneidmiller, S. Schnepp, S. Schreiber, M. Seidel, D. Seratore, A. V. Shabunov, C. Simon, S. Simrock, E. Sombrowski, A. A. Sorokin, P. Spanknebel, R. Spesyvtsev, L. Staykov, B. Steffen, F. Stephan, F. Stulle, H. Thom, K. Tiedtke, M. Tischer, S. Toleikis, R. Treusch, D. Trines, I. Tsakov, E. Vogel, T. Weiland, H. Weise, M. Wellhöfer, M. Wendt, I. Will, A. Winter, K. Wittenburg, W. Wurth, P. Yeates, M. V. Yurkov, I. Zagorodnov, and K. Zapfe, "Operation of a free-electron laser from the extreme ultraviolet to the water window," *Nat. Photon.* **1**, 336–342 (2007).
- <sup>20</sup>T. Tschentscher, C. Bressler, J. Grünert, A. Madsen, A. P. Mancuso, M. Meyer, A. Scherz, H. Sinn, and U. Zastra, "Photon beam transport and scientific instruments at the European XFEL," *Appl. Sci.* **7**, 592 (2017).
- <sup>21</sup>R. W. Schoenlein, "New science opportunities enabled by LCLS-II x-ray lasers," (2015).
- <sup>22</sup>L. Young, K. Ueda, M. Gühr, P. H. Bucksbaum, M. Simon, S. Mukamel, N. Rohringer, K. C. Prince, C. Masciovecchio, M. Meyer, A. Rudenko, D. Rolles, C. Bostedt, M. Fuchs, D. A. Reis, R. Santra, H. Kapteyn, M. Murnane, H. Ibrahim, F. Légaré, M. J. J. Vrakking, M. Isinger, D. Kroon, M. Gisselbrecht, A. L'Huillier, H. J. Wörner, and S. R. Leone, "Roadmap of ultrafast x-ray atomic and molecular physics," *J. Phys. B* **51**, 032003 (2018).
- <sup>23</sup>K. Tiedtke, A. Azima, N. von Barga, L. Bittner, S. Bonfigt, S. Düsterer, B. Faatz, U. Frühling, M. Gensch, C. Gerth, N. Guerassimova, U. Hahn, T. Hans, M. Hesse, K. Honkavaara, U. Jastrow, P. Juranic, S. Kapitzki, B. Keitel, T. Kracht, M. Kuhlmann, W. B. Li, M. Martins, T. Nuñez, E. Plönjes, H. Redlin, E. L. Saldin, E. A. Schneidmiller, J. R. Schneider, S. Schreiber, N. Stojanovic, F. Tavella, S. Toleikis, R. Treusch, H. Weigelt, M. Wellhöfer, H. Wabnitz, M. V. Yurkov, and J. Feldhaus, "The soft x-ray free-electron laser FLASH at DESY: beamlines, diagnostics and end-stations," *New J. Phys.* **11**, 023029 (2009).
- <sup>24</sup>P. Emma, R. Akre, J. Arthur, R. Bionta, C. Bostedt, J. Bozek, A. Brachmann, P. Bucksbaum, R. Coffee, F. J. Decker, Y. Ding, D. Dowell, S. Edstrom, A. Fisher, J. Frisch, S. Gilevich, J. Hastings, G. Hays, P. Hering, Z. Huang, R. Iverson, H. Loos, M. Messerschmidt, A. Miahnahri, S. Moeller, H. D. Nuhn, G. Pile, D. Ratner, J. Rzepiela, D. Schultz, T. Smith, P. Stefan, H. Tompkins, J. Turner, J. Welch, W. White, J. Wu, G. Yocky, and J. Galayda, "First lasing and operation of an ångström-wavelength free-electron laser," *Nat. Photon.* **4**, 641–647 (2010).
- <sup>25</sup>H. Franz, O. Leupold, R. Röhlsberger, S. V. Roth, O. H. Seeck, J. Spengler, J. Stempfner, M. Tischer, J. Viefhaus, E. Weckert, and T. Wroblewski, "Technical report: PETRA III: DESY's new high brilliance third generation synchrotron radiation source," *Synchrotron Radiat. News* **19**, 25–29 (2006).
- <sup>26</sup>G. Cerullo and S. De Silvestri, "Ultrafast optical parametric amplifiers," *Rev. Sci. Instrum.* **74**, 1–18 (2003).
- <sup>27</sup>M. Musheghyan, P. P. Geetha, D. Faccial, A. Pusala, G. Crippa, A. Campolo, A. G. Ciriolo, M. Devetta, A. Assion, C. Manzoni, C. Vozzi, and S. Stagira, "Tunable, few-cycle, CEP-stable mid-IR optical parametric amplifier for strong field applications," *J. Phys. B* **53**, 185402 (2020).
- <sup>28</sup>K. Mecseki, M. K. R. Windeler, A. Miahnahri, J. S. Robinson, A. M. Fraser, A. R. Fry, and F. Tavella, "High average power 88 W OPCA system for high-repetition-rate experiments at the LCLS x-ray free-electron laser," *Opt. Lett.* **44**, 1257–1260 (2019).
- <sup>29</sup>B. Wolter, M. G. Pullen, M. Baudisch, M. Sclafani, M. Hemmer, A. Senftleben, C. D. Schröter, J. Ullrich, R. Moshhammer, and J. Biegert, "Strong-field physics with mid-IR fields," *Phys. Rev. X* **5**, 021034 (2015), arXiv:1506.03636 [physics].
- <sup>30</sup>F. Krausz and M. Ivanov, "Attosecond physics," *Rev. Mod. Phys.* **81**, 163 (2009).
- <sup>31</sup>M. Nisoli, P. Decleva, F. Calegari, A. Palacios, and F. Martín, "Attosecond electron dynamics in molecules," *Chem. Rev.* **117**, 10760 – 10825 (2017).
- <sup>32</sup>F. Calegari, D. Ayuso, A. Trabattini, L. Belshaw, S. De Camillis, S. Anumula, F. Frassetto, L. Poletto, A. Palacios, P. Decleva, J. B. Greenwood, F. Martín, and M. Nisoli, "Ultrafast electron dynamics in phenylalanine initiated by attosecond pulses," *Science* **346**, 336–339 (2014).
- <sup>33</sup>L. Strüder, S. Epp, D. Rolles, R. Hartmann, P. Holl, G. Lutz, H. Soltau, R. Eckart, C. Reich, K. Heinzinger, C. Thamm, A. Rudenko, F. Krasniqi, K. Kühnel, C. Bauer, C.-D. Schroeter, R. Moshhammer, S. Techert, D. Miessner, M. Porro, O. Haelker, N. Meidinger, N. Kimmel, R. Andritschke, F. Schopper, G. Weidenspointner, A. Ziegler, D. Pietschner, S. Herrmann, U. Pietsch, A. Walenta, W. Leitenberger, C. Bostedt, T. Moeller, D. Rupp, M. Adolph, H. Graafsma, H. Hirsemann, K. Gaertner, R. Richter, L. Foucar, R. L. Shoeman, I. Schlichting, and J. Ullrich, "Large-format, high-speed, x-ray pnCCDs combined with electron and ion imaging spectrometers in a multipurpose chamber for experiments at 4th generation light sources," *Nucl. Instrum. Methods Phys. Res. A* **614**, 483–496 (2010).
- <sup>34</sup>H. N. Chapman, "X-ray imaging beyond the limits," *Nature Mater.* **8**, 299–301 (2009).
- <sup>35</sup>H. N. Chapman, P. Fromme, A. Barty, T. A. White, R. A. Kirian, A. Aquila, M. S. Hunter, J. Schulz, D. P. Deponte, U. Weierstall, R. B. Doak, F. R. N. C. Maia, A. V. Martin, I. Schlichting, L. Lomb, N. Coppola, R. L. Shoeman, S. W. Epp, R. Hartmann, D. Rolles, A. Rudenko, L. Foucar, N. Kimmel, G. Weidenspointner, P. Holl, M. Liang, M. Barthelmeß, C. Caleman, S. Boutet, M. J. Bogan, J. Krzywinski, C. Bostedt, S. Bajt, L. Gumprecht, B. Rudek, B. Erk, C. Schmidt, A. Hömke, C. Reich, D. Pietschner, L. Strüder, G. Hauser, H. Gorke, J. Ullrich, S. Herrmann, G. Schaller, F. Schopper, H. Soltau, K.-U. Kühnel, M. Messerschmidt, J. D. Bozek, S. P. Hau-Riege, M. Frank, C. Y. Hampton, R. G. Sierra, D. Starodub, G. J. Williams, J. Hajdu, N. Timneanu, M. M. Seibert, J. Andreasson, A. Rucker, O. Jönsson, M. Svenda, S. Stern, K. Nass, R. Andritschke, C.-D. Schröter, F. Krasniqi, M. Bott, K. E. Schmidt, X. Wang, I. Grothjohann, J. M. Holton, T. R. M. Barends, R. Neutze, S. Marchesini, R. Fromme, S. Schorb, D. Rupp, M. Adolph, T. Gorkhovei, I. Andersson, H. Hirsemann, G. Potdevin, H. Graafsma, B. Nilsson, and J. C. H. Spence, "Femtosecond x-ray protein nanocrystallography,"

- Nature **470**, 73–77 (2011).
- <sup>36</sup>J. Woodhouse, G. N. Kovacs, N. Coquelle, L. M. Uriarte, V. Adam, T. R. M. Barends, M. Byrdin, E. d. I. Mora, R. B. Doak, M. Feliks, M. Field, F. Fieschi, V. Guillon, S. Jakobs, Y. Joti, P. Macheboeuf, K. Motomura, K. Nass, S. Owada, C. M. Roome, C. Ruckebusch, G. Schirò, R. L. Shoeman, M. Thepaut, T. Togashi, K. Tono, M. Yabashi, M. Cammarata, L. Foucar, D. Bourgeois, M. Sliwa, J.-P. Colletier, I. Schlichting, and M. Weik, “Photoswitching mechanism of a fluorescent protein revealed by time-resolved crystallography and transient absorption spectroscopy,” Nat. Commun. **11**, 741 (2020).
- <sup>37</sup>A. Barty, J. Küpper, and H. N. Chapman, “Molecular imaging using x-ray free-electron lasers,” Annu. Rev. Phys. Chem. **64**, 415–435 (2013).
- <sup>38</sup>L. Young, E. P. Kanter, B. Kraessig, Y. Li, A. M. March, S. T. Pratt, R. Santra, S. H. Southworth, N. Rohringer, L. F. DiMauro, G. Doumy, C. A. Roedig, N. Berrah, L. Fang, M. Hoener, P. H. Bucksbaum, J. P. Cryan, S. Ghimire, J. M. Glowia, D. A. Reis, J. D. Bozek, C. Bostedt, and M. Messerschmidt, “Femtosecond electronic response of atoms to ultra-intense x-rays,” Nature **466**, 56 (2010).
- <sup>39</sup>B. Rudek, S.-K. Son, L. Foucar, S.-W. Epp, B. Erk, R. Hartmann, M. Adolph, R. Andritschke, A. Aquila, N. Berrah, C. Bostedt, N. Bozek, Johann Coppola, F. Filsinger, H. Gorke, T. Gorkhova, H. Graafsma, L. Gumprecht, A. Hartmann, G. Hauser, S. Herrmann, H. Hirschmann, P. Holl, A. Hömke, L. Journal, C. Kaiser, N. Kimmel, F. Krasnqi, K.-U. Kühnel, M. Matysek, M. Messerschmidt, D. Miesner, T. Möller, R. Moshhammer, K. Nagaya, B. Nilsson, G. Potdevin, D. Pietschner, C. Reich, D. Rupp, G. Schaller, I. Schlichting, C. Schmidt, F. Schopper, S. Schorb, C.-D. Schröter, S. Schulz, M. Simon, H. Soltau, L. Strüder, K. Ueda, G. Weidenspointner, R. Santra, J. Ullrich, A. Rudenko, and D. Rolles, “Ultra-efficient ionization of heavy atoms by intense x-ray free-electron laser pulses,” Nat. Photon. **6**, 858–865 (2012).
- <sup>40</sup>U. Eichmann, H. Rottke, S. Meise, J.-E. Rubensson, J. Söderström, M. Agåker, C. Sätze, M. Meyer, T. M. Baumann, R. Boll, A. D. Fanis, P. Grychtol, M. Ilchen, T. Mazza, J. Montano, V. Music, Y. Ovcharenko, D. E. Rivas, S. Serkez, R. Wagner, and S. Eisebitt, “Photon-recoil imaging: Expanding the view of nonlinear x-ray physics,” Science **369**, 1630–1633 (2020).
- <sup>41</sup>X. Li, L. Inhester, S. J. Robotjazi, B. Erk, R. Boll, K. Hanasaki, K. Toyota, Y. Hao, C. Bomme, B. Rudek, L. Foucar, S. H. Southworth, C. S. Lehmann, B. Kraessig, T. Marchenko, M. Simon, K. Ueda, K. R. Ferguson, M. Bucher, T. Gorkhover, S. Caron, R. Alonso-Mori, J. E. Koglin, J. Correa, G. J. Williams, S. Boutet, L. Young, C. Bostedt, S.-K. Son, R. Santra, D. Rolles, and A. Rudenko, “Pulse energy and pulse duration effects in the ionization and fragmentation of iodomethane by ultraintense hard x rays,” Phys. Rev. Lett. **127**, 093202 (2021).
- <sup>42</sup>K. Fehre, N. M. Novikovskiy, S. Grundmann, G. Kastirke, S. Eckart, F. Trinter, J. Rist, A. Hartung, D. Trabert, C. Janke, G. Nalin, M. Pitzer, S. Zeller, F. Wiegandt, M. Weller, M. Kircher, M. Hofmann, L. P. H. Schmidt, A. Knie, A. Hans, L. B. Ltaief, A. Ehresmann, R. Berger, H. Fukuzawa, K. Ueda, H. Schmidt-Böcking, J. B. Williams, T. Jahnke, R. Dörner, M. S. Schöffler, and P. V. Demekhin, “Fourfold differential photoelectron circular dichroism,” Phys. Rev. Lett. **127**, 103201 (2021).
- <sup>43</sup>J. W. L. Lee, D. S. Tikhonov, P. Chopra, S. Maclot, A. L. Steber, S. Gruet, F. Allum, R. Boll, X. Cheng, S. Düsterer, B. Erk, D. Garg, L. He, D. Heathcote, M. Johny, M. M. Kazemi, H. Köckert, J. Lahl, A. K. Lemmens, D. Loru, R. Mason, E. Müller, T. Mullins, P. Olshin, C. Passow, J. Peschel, D. Ramm, D. Rompotis, N. Schirmel, S. Trippel, J. Wiese, F. Ziaee, S. Bari, M. Burt, J. Küpper, A. M. Rijs, D. Rolles, S. Techert, P. Eng-Johnsson, M. Brouard, C. Vallance, B. Manschwetus, and M. Schnell, “Time-resolved relaxation and fragmentation of polycyclic aromatic hydrocarbons investigated in the ultrafast XUV-IR regime,” Nat. Commun. **12**, 6107 (2021).
- <sup>44</sup>L. Dunoyer, “Sur la théorie cinétique des gaz et la réalisation d’un rayonnement matériel d’origine thermique,” Cf. hebdomadaire Acad. sci. **152**, 592–595 (1911).
- <sup>45</sup>R. G. J. Fraser, *Molecular Rays* (Cambridge University Press, London, GB, 1931).
- <sup>46</sup>D. R. Herschbach, “Reactive collisions in crossed molecular beams,” Discuss. Faraday Soc. **33**, 149–161 (1962).
- <sup>47</sup>L. D. Carr, D. DeMille, R. V. Krems, and J. Ye, “Cold and ultracold molecules: science, technology and applications,” New J. Phys. **11**, 055049 (2009).
- <sup>48</sup>S. Y. T. van de Meerakker, H. L. Bethlem, and G. Meijer, “Taming molecular beams,” Nat. Phys. **4**, 595 (2008).
- <sup>49</sup>M. Fárnik, “Bridging gaps between clusters in molecular-beam experiments and aerosol nanoclusters,” J. Phys. Chem. Lett. **14**, 287–294 (2023).
- <sup>50</sup>Y.-P. Chang, D. A. Horke, S. Trippel, and J. Küpper, “Spatially-controlled complex molecules and their applications,” Int. Rev. Phys. Chem. **34**, 557–590 (2015), arXiv:1505.05632 [physics].
- <sup>51</sup>A. A. Milner, J. A. M. Fordyce, I. MacPhail-Bartley, W. Wasserman, V. Milner, I. Tutunnikov, and I. S. Averbukh, “Controlled enantioselective orientation of chiral molecules with an optical centrifuge,” Phys. Rev. Lett. **122**, 223201 (2019).
- <sup>52</sup>S. Beaulieu, A. Comby, A. Clergerie, J. Caillat, D. Descamps, N. Dudovich, B. Fabre, R. Généaux, F. Lègaré, S. Petit, B. Pons, G. Porat, T. Ruchon, R. Taïeb, V. Blanchet, and Y. Mairesse, “Attosecond-resolved photoionization of chiral molecules,” Science **358**, 1288–1294 (2017).
- <sup>53</sup>J. Onvlee, S. Trippel, and J. Küpper, “Ultrafast light-induced dynamics in solvated biomolecules: The indole chromophore with water,” Nat. Commun. **13**, 7462 (2022), arXiv:2103.07171 [physics].
- <sup>54</sup>M. Johny, C. A. Schouder, A. Al-Refaie, L. He, J. Wiese, H. Stapelfeldt, S. Trippel, and J. Küpper, “Water is a radiation protection agent for ionised pyrrole,” Phys. Chem. Chem. Phys. **26**, 13118–13130 (2024), arXiv:2010.00453 [physics].
- <sup>55</sup>F. Filsinger, U. Erlekam, G. von Helden, J. Küpper, and G. Meijer, “Selector for structural isomers of neutral molecules,” Phys. Rev. Lett. **100**, 133003 (2008), arXiv:0802.2795 [physics].
- <sup>56</sup>F. Filsinger, J. Küpper, G. Meijer, J. L. Hansen, J. Maurer, J. H. Nielsen, L. Holmegaard, and H. Stapelfeldt, “Pure samples of individual conformers: The separation of stereo-isomers of complex molecules using electric fields,” Angew. Chem. Int. Ed. **48**, 6900–6902 (2009).
- <sup>57</sup>S. Trippel, Y.-P. Chang, S. Stern, T. Mullins, L. Holmegaard, and J. Küpper, “Spatial separation of state- and size-selected neutral clusters,” Phys. Rev. A **86**, 033202 (2012), arXiv:1208.4935 [physics].
- <sup>58</sup>D. A. Horke, Y.-P. Chang, K. Długołęcki, and J. Küpper, “Separating para and ortho water,” Angew. Chem. Int. Ed. **53**, 11965–11968 (2014), arXiv:1407.2056 [physics].
- <sup>59</sup>N. Teschmit, D. A. Horke, and J. Küpper, “Spatially separating the conformers of a dipeptide,” Angew. Chem. Int. Ed. **57**, 13775–13779 (2018), arXiv:1805.12396 [physics].
- <sup>60</sup>J. Ullrich, R. Moshhammer, A. Dorn, R. Dörner, L. P. H. Schmidt, and H. Schmidt-Böcking, “Recoil-ion and electron momentum spectroscopy: Reaction-microscopes,” Rep. Prog. Phys. **66**, 1463–1545 (2003).
- <sup>61</sup>A. T. J. B. Eppink and D. H. Parker, “Velocity map imaging of ions and electrons using electrostatic lenses: Application in photoelectron and photofragment ion imaging of molecular oxygen,” Rev. Sci. Instrum. **68**, 3477–3484 (1997).
- <sup>62</sup>L. J. Frasinski, K. Codling, and P. A. Hatherly, “Covariance mapping: a correlation method applied to multiphoton multiple ionization,” Science **246**, 1029–1031 (1989).
- <sup>63</sup>A. Bodi, P. Hemberger, T. Gerber, and B. Sztáray, “A new double imaging velocity focusing coincidence experiment:  $i^2$ PEPICO,” Rev. Sci. Instrum. **83**, 083105 (2012).
- <sup>64</sup>U. Even, “The Even-Lavie valve as a source for high intensity supersonic beam,” Eur. Phys. J. Techn. Instrumen. **2**, 17 (2015).
- <sup>65</sup>A. Al-Refaie, M. Johny, J. Correa, D. Pennicard, P. Svihra, A. Nomerotski, S. Trippel, and J. Küpper, “PymePix: A Python library for SPIDR readout of Timepix3,” J. Instrum. **14**, P10003 (2019), arXiv:1905.07999 [physics].

- <sup>66</sup>H. Bromberger, C. Passow, D. Pennicard, R. Boll, J. Correa, L. He, M. Johny, C. Papadopoulou, A. Tul-Noor, J. Wiese, S. Trippel, B. Erk, and J. Küpper, “Shot-by-shot 250 kHz 3D ion and MHz photoelectron imaging using Timepix3,” *J. Phys. B* **55**, 144001 (2022), arXiv:2111.14407 [physics].
- <sup>67</sup>A. Zhao, M. van Beuzekom, B. Bouwens, D. Byelov, I. Chakaberia, C. Cheng, E. Maddox, A. Nomerotski, P. Svihra, J. Visser, V. Vrba, and T. Weinacht, “Coincidence velocity map imaging using Tpx3Cam, a time stamping optical camera with 1.5 ns timing resolution,” *Rev. Sci. Instrum.* **88**, 113104 (2017), arXiv:1707.06253 [physics].
- <sup>68</sup>A. Tremsin and J. Vallergera, “Unique capabilities and applications of microchannel plate (MCP) detectors with Medipix/Timepix readout,” *Radiat. Meas.* **130**, 106228 (2020).
- <sup>69</sup>D. Wood, R. J. Burleigh, N. Smith, D. Bortoletto, M. Brouard, M. Burt, A. Nomerotski, R. Plackett, and I. Shipsey, “Ion microscope imaging mass spectrometry using a Timepix3-based optical camera,” *J. Am. Soc. Mass Spectrom.* **33**, 2328–2332 (2022).
- <sup>70</sup>J. Küpper, H. Haak, K. Wohlfart, and G. Meijer, “Compact in-place gate valve for molecular-beam experiments,” *Rev. Sci. Instrum.* **77**, 016106 (2006).
- <sup>71</sup>S. Trippel, T. G. Mullins, N. L. M. Müller, J. S. Kienitz, K. Długołęcki, and J. Küpper, “Strongly aligned and oriented molecular samples at a kHz repetition rate,” *Mol. Phys.* **111**, 1738 (2013), arXiv:1301.1826 [physics].
- <sup>72</sup>J. S. Kienitz, K. Długołęcki, S. Trippel, and J. Küpper, “Improved spatial separation of neutral molecules,” *J. Chem. Phys.* **147**, 024304 (2017), arXiv:1704.08912 [physics].
- <sup>73</sup>F. Filsinger, J. Küpper, G. Meijer, L. Holmegaard, J. H. Nielsen, I. Nevo, J. L. Hansen, and H. Stapelfeldt, “Quantum-state selection, alignment, and orientation of large molecules using static electric and laser fields,” *J. Chem. Phys.* **131**, 064309 (2009), arXiv:0903.5413 [physics].
- <sup>74</sup>S. Trippel, M. Johny, T. Kierspel, J. Onvlee, H. Bieker, H. Ye, T. Mullins, L. Gumprecht, K. Długołęcki, and J. Küpper, “Knife edge skimming for improved separation of molecular species by the deflector,” *Rev. Sci. Instrum.* **89**, 096110 (2018), arXiv:1802.04053 [physics].
- <sup>75</sup>B. van der Heijden, J. Visser, M. van Beuzekom, H. Boterenbrood, S. Kulis, B. Munneke, and F. Schreuder, “SPIDR, a general-purpose readout system for pixel ASICs,” *J. Instrum.* **12**, C02040 (2017).
- <sup>76</sup>M. Takahashi, J. P. Cave, and J. H. D. Eland, “Velocity imaging photoionization coincidence apparatus for the study of angular correlations between electrons and fragment ions,” *Rev. Sci. Instrum.* **71**, 1337–1344 (2000).
- <sup>77</sup>M. Stei, J. von Vangerow, R. Otto, A. H. Kelkar, E. Carrascosa, T. Best, and R. Wester, “High resolution spatial map imaging of a gaseous target,” *J. Chem. Phys.* **138**, 214201 (2013).
- <sup>78</sup>CFEL Controlled Molecule Imaging, “PymePix,” Code repository, URL: <https://gitlab.desy.de/CMI/CMI-public/pymepix> (2024).
- <sup>79</sup>C. Cheng, G. Moğol, T. Weinacht, A. Nomerotski, and C. Trallero-Herrero, “3D velocity map imaging of electrons with TPX3CAM,” *Rev. Sci. Instrum.* **93**, 013003 (2022).
- <sup>80</sup>H. Bromberger, D. Pennicard, R. Ballabriga, S. Trippel, and J. Küpper, “Timepix3: single-pixel multi-hit energy-measurement behavior,” *J. Instrum.* (2024), submitted.
- <sup>81</sup>L. Rading, J. Lahl, S. Maclot, F. Campi, H. Coudert-Alteirac, B. Oostenrijk, J. Peschel, H. Wikmark, P. Rudawski, M. Gisselbrecht, and P. Johnsson, “A versatile velocity map ion-electron covariance imaging spectrometer for high-intensity XUV experiments,” *Appl. Sci.* **8**, 998 (2018), arXiv:1901.03077 [physics].
- <sup>82</sup>J. Wiese, J.-F. Olivieri, A. Trabattoni, S. Trippel, and J. Küpper, “Strong-field photoelectron momentum imaging of OCS at finely resolved incident intensities,” *New J. Phys.* **21**, 083011 (2019), arXiv:1904.07519 [physics].
- <sup>83</sup>S. Trippel, T. Mullins, N. L. M. Müller, J. S. Kienitz, R. González-Férez, and J. Küpper, “Two-state wave packet for strong field-free molecular orientation,” *Phys. Rev. Lett.* **114**, 103003 (2015), arXiv:1409.2836 [physics].
- <sup>84</sup>S. Hankin, D. Villeneuve, P. Corkum, and D. Rayner, “Intense-field laser ionization rates in atoms and molecules,” *Phys. Rev. A* **64**, 013405 (2001).
- <sup>85</sup>M. Yousefi, P. F. Bernath, C. D. Boone, and G. C. Toon, “Global measurements of atmospheric carbonyl sulfide (OCS), OC<sup>34</sup>S and O<sup>13</sup>CS,” *J. Quant. Spectrosc. Radiat. Transf.* **238**, 106554 (2019).
- <sup>86</sup>E. Karamatskos, S. Yarlagadda, S. Patchkovskii, M. Vrakking, R. Welsch, J. Küpper, and A. Rouzée, “Time-resolving the UV-initiated photodissociation dynamics of OCS,” *Faraday Disc.* **228**, 413 (2021), arXiv:2010.09406 [physics].
- <sup>87</sup>F. Allum, V. Music, L. Inhester, R. Boll, B. Erk, P. Schmidt, T. M. Baumann, G. Brenner, M. Burt, P. V. Demekhin, S. Dörner, A. Ehresmann, A. Galler, P. Grychtol, D. Heathcote, D. Kargin, M. Larsson, J. W. L. Lee, Z. Li, B. Manschwetus, L. Marder, R. Mason, M. Meyer, H. Otto, C. Passow, R. Pietschnig, D. Ramm, K. Schubert, L. Schwob, R. D. Thomas, C. Vallance, I. Vidanović, C. v. K. Schmising, R. Wagner, P. Walter, V. Zhaunerchyk, D. Rolles, S. Bari, M. Brouard, and M. Ilchen, “A localized view on molecular dissociation via electron-ion partial covariance,” *Commun. Chem.* **5**, 42 (2022).



**Supporting Information for Publication:****A versatile and transportable endstation for controlled molecule experiments**

Wuwei Jin,<sup>1,2</sup> Hubertus Bromberger,<sup>1</sup> Lanhai He,<sup>1,\*</sup> Melby Johny,<sup>1,2,3</sup> Ivo S. Vinklársek,<sup>1</sup> Karol Długołęcki,<sup>1</sup> Andrey Samartsev,<sup>1</sup> Francesca Calegari,<sup>1,2,3</sup> Sebastian Trippel,<sup>1,3,†</sup> and Jochen Küpper<sup>1,2,3,‡</sup>

<sup>1</sup>*Center for Free-Electron Laser Science CFEL, Deutsches*

*Elektronen-Synchrotron DESY, Notkestr. 85, 22607 Hamburg, Germany*

<sup>2</sup>*Department of Physics, Universität Hamburg, Luruper Chaussee 149, 22761 Hamburg, Germany*

<sup>3</sup>*Center for Ultrafast Imaging, Universität Hamburg, Luruper Chaussee 149, 22761 Hamburg, Germany*

**CONTENTS**

List of Figures	S1
Vacuum system	S1
Interlock system	S1
Detection efficiency	S2

**LIST OF FIGURES**

S1	Vacuum system . . . . .	S2
S2	General concept of the interlock controller. . . . .	S3
S3	Front- (left) and back-panel (right) of the interlock controller. . . . .	S3
S4	Interlock system. . . . .	S4

**VACUUM SYSTEM**

Figure S1 illustrates the vacuum setup, including the high-pressure gas line of the eCOMO system. The source-, deflector-, VMI- and beam-dump chambers are indicated as the light blue structure. The gas flow is depicted by red arrows starting from the Even-Lavie valve in the source chamber. The turbomolecular pumps are indicated as yellow rectangles and are discussed in the main manuscript. The roughing-line pump is indicated as OTB. The automatic gate valves are shown as blue symbols. Here, gate valves 1 and 4 are DN40-ISO-KF mini gate valves (VAT 01232-KA44). Gate valve 3 is a DN16 ISO-KF mini gate valve (VAT 01224-KA44). Gate valve 4 indicates the home-built automatic DN250 CF gate valve [? ], which allows separating the source from the deflector chamber. This gate valve is driven by a solenoid valve (Festo VUVS-LK20-M52-AD-G18-1C1-S). All gate valves are controlled by a home-built NIM-based controller. Vacuum monitoring is accomplished by the gauges shown in Figure S1 as green rectangles (Pfeiffer Vacuum PKR 251, PBR260, and IKR270). All gauges are controlled and monitored by a controller (Pfeiffer TPG 366).

**INTERLOCK SYSTEM**

The general concept of the interlock controller logic is illustrated in Figure S2. The box has 5 two-wire LEMO inputs and 5 one-wire LEMO outputs. One of the two-wire input wires delivers 5 V (Send). The second wire is used to drive the Transistor-Transistor Logic (TTL) driver Integrated Circuits (ICs) labeled as Return in Figure S2. All input channels are connected via push pins with an attachable circuit board in the interlock controller. The push pins can be used to select a specific pin assignment of the input connectors with respect to Send and Return. The Return signal drives two ICs, a TTL driver and an inverted TTL driver, respectively. In this way, the input logic can be inverted making use of the jumpers right behind the TTL drivers. The TTL driver ICs serve in addition as a protection of the interlock controller in terms of over voltages. The attachable circuit board can be easily replaced if necessary since it is connected to a main circuit board via push pins. A CPLD (Complex Programmable Logic Device) is used to logically connect the input signals and interlock hardware switches with the output channels and LEDs. In this way, the logical program can be changed quickly. The output voltage can be switched between 5, 12, and 24 V depending on the specific requirements of the corresponding device attached.

The front- and back panel of the interlock controller are shown in Figure S3. The upper half of the front panel contains LED indicators and switches for the input channels. The lower half of the front panel contains LED indicators and switches to indicate the status and control the output channels. Input and output channels are provided via the back plate of the module. LEDs on the front panel indicate the status of the box depending on the logic of the CPLD.

Figure S4 illustrates how the interlock system monitors and protects the vacuum system. The pressure-gauge controller records the vacuum from each gauge and, depending on whether the respective threshold conditions are met, sends a 5 V trigger signal to the interlock box. The interlock box then processes these input signals and transmits corresponding output trigger signals to the gate valves controller box and electrode power supplies to control their operation. In this special case, a gate valve can only be opened if all

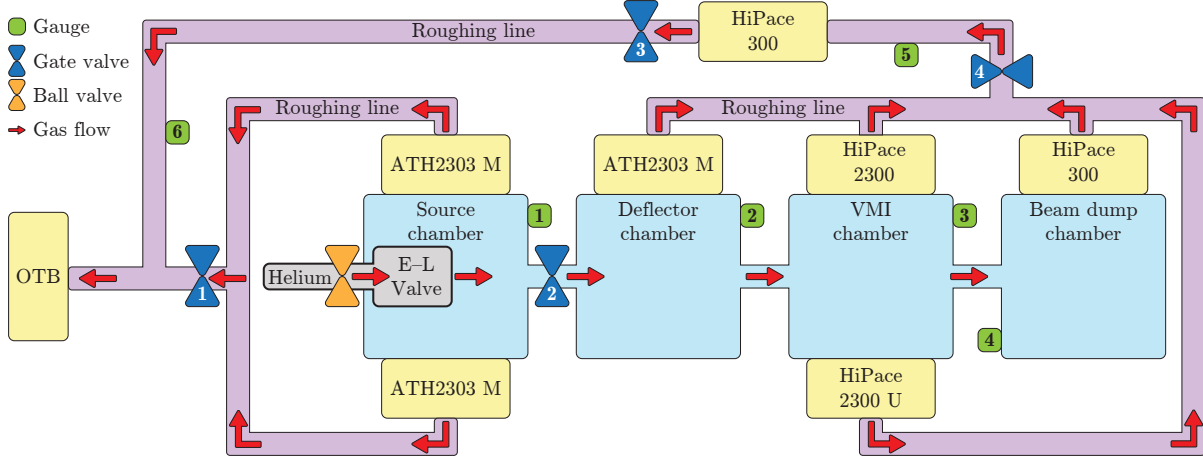


Figure S1. Schematic of the eCOMO vacuum system together with the high pressure gas line. Gauges and pumps are indicated as green and yellow rectangles, respectively. Red arrows depict the gas flow. Ball and gate valves are indicated by orange and blue symbols, respectively. The high-vacuum part of the setup is depicted in light blue. The roughing lines are shown in light purple. The high-pressure line and the Even-Lavie valve (E-L valve) are shown by the gray shaded structure.

vacuum systems connected by this valve are within the permitted pressure range. Additionally, voltage can only be applied to the electrodes when the pressure in the VMI chamber is below the threshold.

## DETECTION EFFICIENCY

The low power correlation measurements used for Figure 5 g in the main manuscript enabled us furthermore to obtain the detection efficiency for electrons and ions in our setup. For each detected electron, we examined whether there was a simultaneous detection of an ion for the same laser shot. The detection

efficiency for ions  $\alpha_i$  and electrons  $\alpha_e$  is given by:

$$\alpha_i = \frac{N_i \cdot N_e - N_{\text{uncor.}}}{N_{|e|>1}}, \alpha_e = \frac{N_i \cdot N_e - N_{\text{uncor.}}}{N_{|i|>1}} \quad (1)$$

Here we have the number of electrons  $N_e$ , the number of ions  $N_i$ , the number of uncorrelated events on both detectors  $N_{\text{uncor.}}$ , the number of ions with at least one detected electron  $N_{|e|>1}$ , and the number of electrons with at least one detected ion  $N_{|i|>1}$ . From our data we obtain a final total detection efficiency of  $\alpha_i = 35.90\%$  and  $\alpha_e = 35.35\%$ . Assuming a detection efficiency of the MCP given by  $\alpha_{\text{MCP}} = 50\%$  we obtain a transparency for a single mesh  $\alpha_{\text{mesh}} = 83.7\%$ , which is in agreement with the nominal transmission of 80%. The deviation is attributed to the fact that the effective transmission of the second grid is higher due to the shadow cast by the first grid.

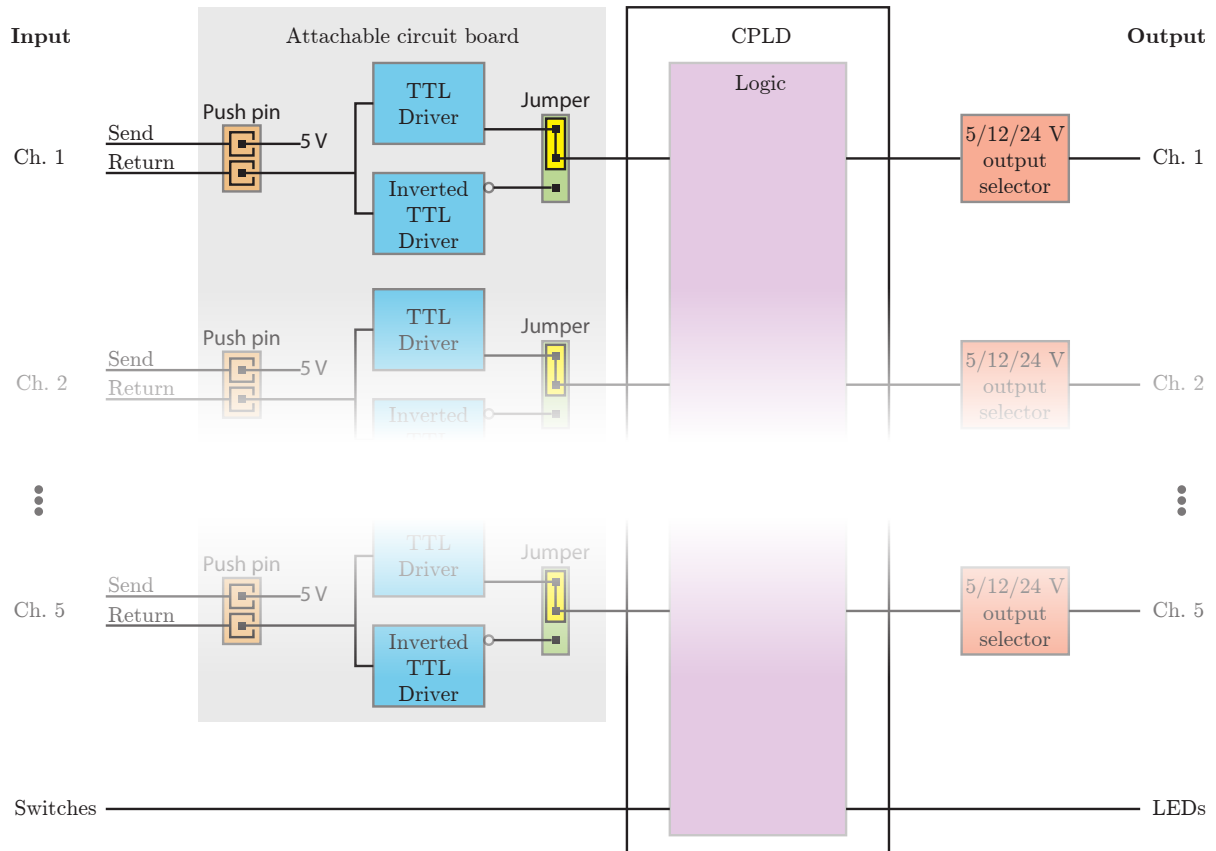


Figure S2. General concept of the interlock controller.



Figure S3. Front- (left) and back-panel (right) of the interlock controller.

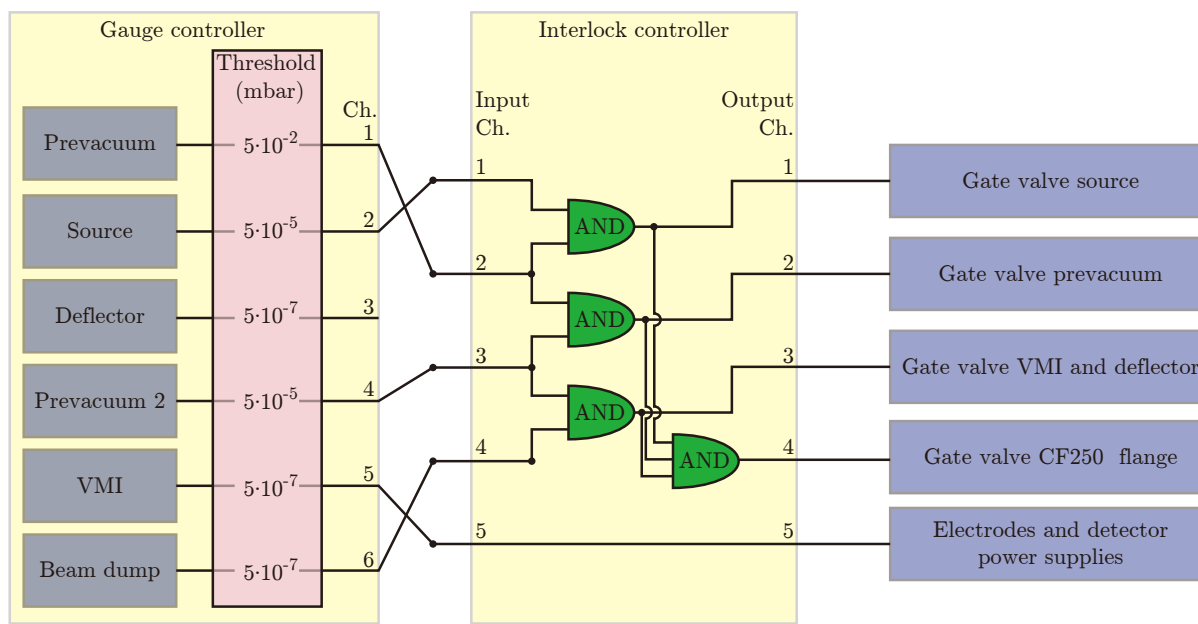


Figure S4. Interlock logic used at eCOMO. Thresholds for pressures are set on the gauge controller on the left. The corresponding outputs are sent to the input of the interlock controller. The CPLD of the interlock controller is programmed as illustrated in the figure. The logic output of the interlock controller drives the gate valves and the logic for the power supplies as indicated on the right.